



Spectroscopy[®]

Solutions for Materials Analysis

June 2018 Volume 33 Number s6

www.spectroscopyonline.com

RAMAN TECHNOLOGY

for Today's Spectroscopists



UBM

Modular SERS System for Trace Level Detection

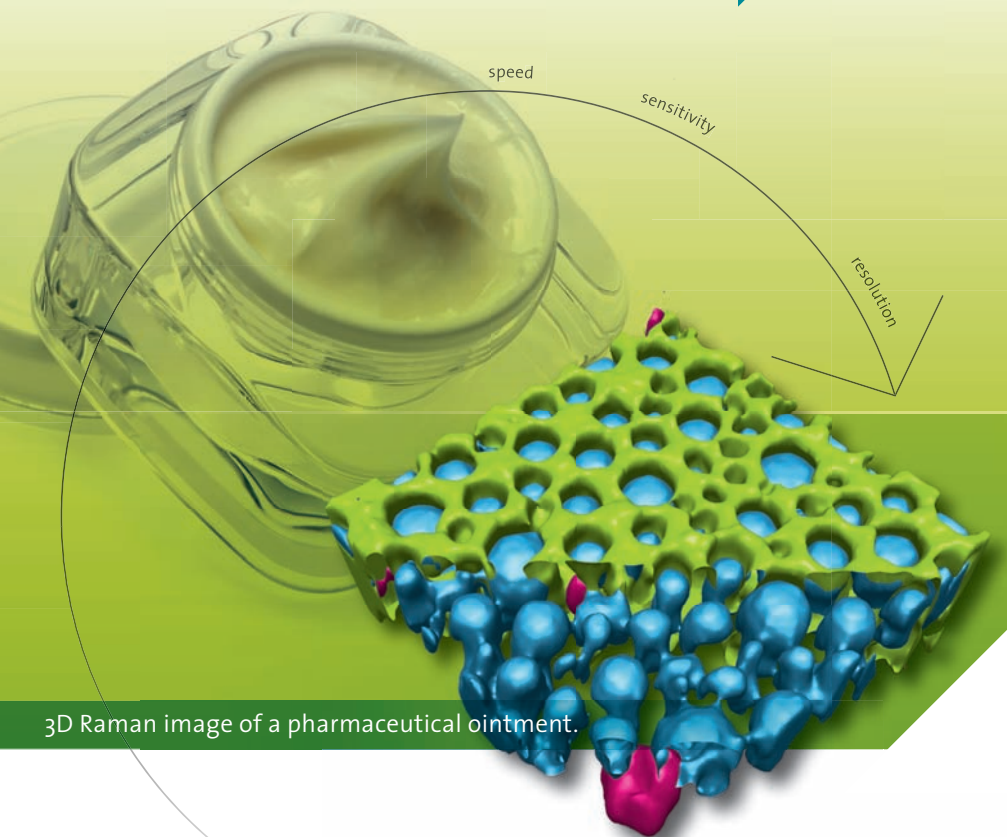
New Sample Holder Makes Measurements Simple

It's easier than ever to configure a SERS system for trace analysis of samples including pesticides, narcotics and food additives.

- ▶ System comprises spectrometer, 785 nm laser excitation, probe and SERS substrate holder
- ▶ Holder secures probe and positions SERS substrates
- ▶ System is compact, reliable and accurate



info@oceanoptics.com
www.oceanoptics.com
US +1 727-733-2447
EUROPE +31 26-3190500
ASIA +86 21-6295-6600



3D Raman image of a pharmaceutical ointment.

3D Raman Imaging

Turn ideas into **discoveries**

Let your discoveries lead the scientific future. Like no other system, WITec's confocal 3D Raman microscopes allow for cutting-edge chemical imaging and correlative microscopy with AFM, SNOM, SEM or Profilometry. Discuss your ideas with us at info@witec.de.



Raman · AFM · SNOM · RISE

www.witec.de

Spectroscopy®

MANUSCRIPTS: To discuss possible article topics or obtain manuscript preparation guidelines, contact the editorial director at: (732) 346-3020, e-mail: Laura.Bush@ubm.com. Publishers assume no responsibility for safety of artwork, photographs, or manuscripts. Every caution is taken to ensure accuracy, but publishers cannot accept responsibility for the information supplied herein or for any opinion expressed.

SUBSCRIPTIONS: For subscription information: *Spectroscopy*, P.O. Box 6196, Duluth, MN 55806-6196; (888) 527-7008, 7:00 a.m. to 6:00 p.m. CST. Outside the U.S., +1-218-740-6477. Delivery of *Spectroscopy* outside the U.S. is 3–14 days after printing. Single-copy price: U.S., \$10.00 + \$7.00 postage and handling (\$17.00 total); Canada and Mexico, \$12.00 + \$7.00 postage and handling (\$19.00 total); Other international, \$15.00 + \$7.00 postage and handling (\$22.00 total).

CHANGE OF ADDRESS: Send change of address to *Spectroscopy*, P.O. Box 6196, Duluth, MN 55806-6196; provide old mailing label as well as new address; include ZIP or postal code. Allow 4–6 weeks for change. Alternately, go to the following URL for address changes or subscription renewal: <http://ubmsubs.ubm.com/?pubid=SPEC>

RETURN ALL UNDELIVERABLE CANADIAN ADDRESSES TO: IMEX Global Solutions, P.O. Box 25542, London, ON N6C 6B2, CANADA. PUBLICATIONS MAIL AGREEMENT No.40612608.

REPRINT SERVICES: Reprints of all articles in this issue and past issues are available (500 minimum). Licensing and Reuse of Content: Contact our official partner, Wright's Media, about available usages, license fees, and award seal artwork at Advanstar@wrightsmedia.com for more information. Please note that Wright's Media is the only authorized company that we've partnered with for Advanstar UBM materials.

C.A.S.T. DATA AND LIST INFORMATION: Contact Melissa Stillwell, (218) 740-6831; e-mail: Melissa.Stillwell@ubm.com

INTERNATIONAL LICENSING: Jillyn Frommer, (732) 346-3007, fax: (732) 647-1104; e-mail: Jillyn.Frommer@ubm.com

© 2018 UBM. All rights reserved. No part of this publication may be reproduced or transmitted in any form or by any means, electronic or mechanical including by photocopy, recording, or information storage and retrieval without permission in writing from the publisher. Authorization to photocopy items for internal/educational or personal use, or the internal/educational or personal use of specific clients is granted by UBM for libraries and other users registered with the Copyright Clearance Center, 222 Rosewood Dr. Danvers, MA 01923, 978-750-8400 fax 978-646-8700 or visit <http://www.copyright.com> online. For uses beyond those listed above, please direct your written request to Permission Dept. fax 732-647-1104 or email: Jillyn.Frommer@ubm.com.

UBM Americas provides certain customer contact data (such as customers' names, addresses, phone numbers, and e-mail addresses) to third parties who wish to promote relevant products, services, and other opportunities that may be of interest to you. If you do not want UBM Americas to make your contact information available to third parties for marketing purposes, simply call toll-free 866-529-2922 between the hours of 7:30 a.m. and 5 p.m. CST and a customer service representative will assist you in removing your name from UBM Americas lists. Outside the U.S., please phone 218-740-6477.

Spectroscopy does not verify any claims or other information appearing in any of the advertisements contained in the publication, and cannot take responsibility for any losses or other damages incurred by readers in reliance of such content.

Spectroscopy welcomes unsolicited articles, manuscripts, photographs, illustrations and other materials but cannot be held responsible for their safekeeping or return.

To subscribe, call toll-free 888-527-7008. Outside the U.S. call 218-740-6477.

UBM Americas (www.ubmamericas.com) is a leading worldwide media company providing integrated marketing solutions for the Fashion, Life Sciences and Powersports industries. UBM Americas serves business professionals and consumers in these industries with its portfolio of 91 events, 67 publications and directories, 150 electronic publications and Web sites, as well as educational and direct marketing products and services. Market leading brands and a commitment to delivering innovative, quality products and services enables UBM Americas to "Connect Our Customers With Theirs." UBM Americas has approximately 1000 employees and currently operates from multiple offices in North America and Europe.

485F US Highway One South, Suite 210,
Iselin, NJ 08830
(732) 596-0276
Fax: (732) 647-1235

Michael J. Tessalone
Vice President/Group Publisher
Michael.Tessalone@ubm.com

Stephanie Shaffer
Publisher,
Stephanie.Shaffer@ubm.com
(774) 249-1890

Edward Fantuzzi
Associate Publisher,
Edward.Fantuzzi@ubm.com

Michael Kushner
Senior Director, Digital Media
Michael.Kushner@ubm.com

Laura Bush
Editorial Director,
Laura.Bush@ubm.com

Megan L'Heureux
Managing Editor,
Meg.L'Heureux@ubm.com

Stephen A. Brown
Group Technical Editor,
Stephen.Brown@ubm.com

Cindy Delonas
Associate Editor,
Cindy.Delonas@ubm.com

Kristen Moore
Webcast Operations Manager
Kristen.Moore@ubm.com

Vania Oliveira
Project Manager
Vania.Oliveira@ubm.com

Sabina Advani
Digital Production Manager
Sabina.Advani@ubm.com

Kaylynn Chiarello-Ebner
Managing Editor, Special Projects
Kaylynn.Chiarello.Ebner@ubm.com

Dan Ward
Art Director,
dward@hcl.com

Anne Lavigne
Marketing Manager,
Anne.Lavigne@ubm.com

Melissa Stillwell
C.A.S.T. Data and List Information,
Melissa.Stillwell@ubm.com

Thomas W. Ehardt
Executive Vice-President, Senior Managing Director
UBM Life Sciences Group

Dave Esola
VP & General Manager
UBM Life Sciences Group

Jillyn Frommer
Permissions,
Jillyn.Frommer@ubm.com

Jesse Singer
Production Manager,
jsinger@hcl.com

Wendy Bong
Audience Development Manager,
Wendy.Bong@ubm.com

Ross Burns
Audience Development Assistant Manager,
Ross.Burns@ubm.com

Kaiser Raman: trusted from laboratory to process

The **RAMANRXN SYSTEMS™** family of analyzers from Kaiser are robust, reliable and proven in chemical, pharmaceutical, bioprocessing and polymer applications. They are equally suited for operating within the laboratory as a research tool, in a QA/QC laboratory, in process development or in manufacturing.



Research



Process Development



Early Development



Production/ Manufacturing

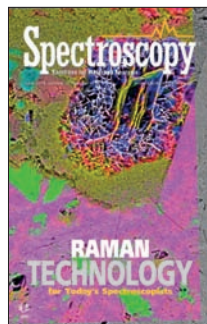


KAISER
OPTICAL SYSTEMS, INC.

An Endress+Hauser Company

www.kosi.com





RAMAN TECHNOLOGY FOR TODAY'S SPECTROSCOPISTS

JUNE 2018 VOLUME 33 NUMBER 6

Articles

8 **Portable Raman Spectroscopy for At-Line Characterization of Carbon Nanomaterials**

Dawn Yang and Kristen Frano

Raman spectroscopy is ideal for at-line or online material analysis for manufacturers of graphene and other carbon nanomaterials to do materials characterization, product quality control, and process monitoring.

20 **Gaining Insight into Cocoa Butter Polymorph Formation Through In Situ Rheology and Raman Spectroscopy**

Nathan C. Crawford, Mohammed Ibrahim, and Rui Chen

The hyphenation of rheology and Raman spectroscopy enabled a more holistic depiction of the crystallization process and provided unique insights into the formation of cocoa butter polymorph form IV.

34 **Data-Driven Raman Spectroscopy in Oil and Gas: Rapid Online Analysis of Complex Gas Mixtures**

Da Chen and Cicely Rathmell

This new data-driven Raman spectroscopy (DDRS) method is capable of simultaneously measuring 12 hydrocarbon and nonhydrocarbon gases in the presence of matrix interferences.

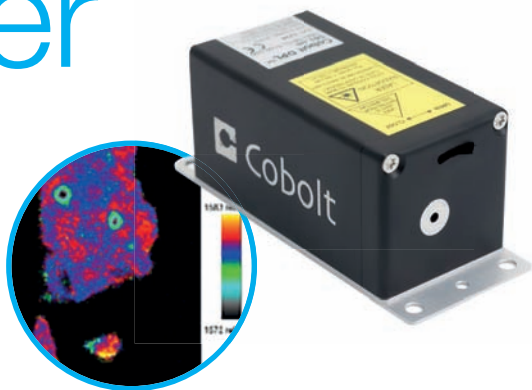
44 **Exploring the Unknown with Correlative Raman Imaging and Scanning Electron Microscopy**

Guillaume Wille, Karin Hollricher, and Ute Schmidt

Confocal Raman imaging and scanning electron microscopy are techniques that are ideally suited to correlating structural and chemical information as shown here on a variety of samples.

See things clearer

with Cobolt



High Performance Lasers For Raman

- 355 nm – 1064 nm
- Single frequency, excellent wavelength stability
- HTCure™ for unprecedented reliability

Portable Raman Spectroscopy for At-Line Characterization of Carbon Nanomaterials

Largely heralded as a “wonder material” since its discovery in 2004, graphene has now entered the era of industrial manufacturing. Although several techniques for large-scale graphene manufacturing have been developed, one important question remains: how to easily and rapidly characterize the quality of graphene and other carbon nanomaterials to effectively monitor and control the production process, where simple and robust analytical tools are required. In this study, three types of materials (graphene powders, graphene powder coated sheets, and carbon nanofibers) were analyzed using portable Raman spectroscopy. This efficient analysis is ideal for at-line or online material analysis for manufacturers of graphene and other carbon nanomaterials to do materials characterization, product quality control, and process monitoring.

Dawn Yang and Kristen Frano

Carbon nanomaterials constitute a variety of carbon allotropes including graphene, graphene oxide, carbon nanotubes, and carbon nanofibers. Each of these materials exhibits unique properties in electrical conductivity, thermal conductivity, and mechanical strength thanks to the distinct structures of each allotrope. For instance, graphene is a two-dimensional (2D) material formed from a hexagonal lattice of carbon atoms, whereas graphite is made up of stacked individual layers of graphene. Graphene's strength, superconductivity, and excellent heat conductivity makes it a very attractive material as a conductor in memory chips and batteries for electronics (1), and its flexibility has the potential

to invigorate infrastructure, aeronautics, and biotechnology. Graphene oxide, an alternative form of graphene made from oxidized graphite that has been exfoliated to form a few layers or a single layer, is used to desalinate water and remove radioactive isotopes (2). Carbon nanotubes, which are tubes with walls formed from graphene sheets, have attracted interest from industry to potentially generate high-surface-area catalysts in fuel cells with the addition of different functional groups (3). Carbon nanotubes can either be single-walled nanotubes (SWNTs) or multiwalled nanotubes (MWNTs). Recently, MWNTs have found practical use in lithium-ion batteries to increase the lifespan and capacity of portable elec-



What did you do today?

Whether you're discovering new materials, solving analytical problems or assuring product quality, your spectrometer needs to deliver the definitive answers you're looking for — fast! Thermo Fisher Scientific goes beyond your expectations with a full line of FTIR, NIR and Raman spectroscopy systems to help you move from sample to answer, faster than ever before.

With the Thermo Scientific™ DXR™2xi Raman Imaging Microscope, you get an easy-to-use system that rapidly delivers accurate data – so you spend less time concentrating on measurement and more time on scientific discovery.

Discover. Solve. Assure.
thermofisher.com/discover-dxr

ThermoFisher
SCIENTIFIC

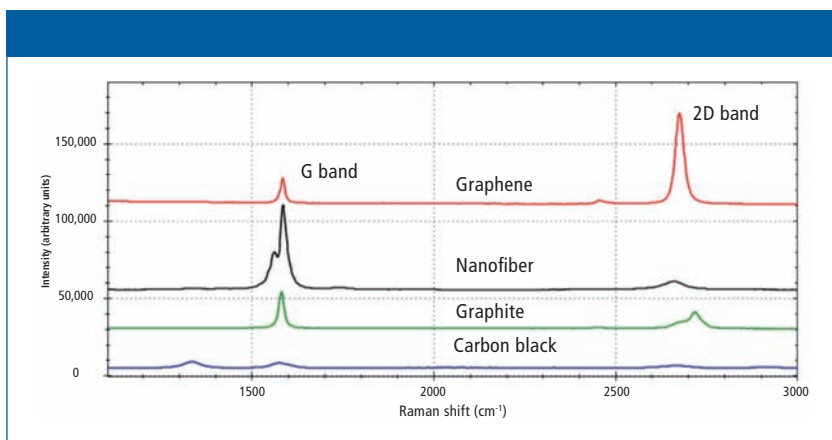


Figure 1: Raman spectra of graphene (red), carbon nanotubes (black), graphite (green), and carbon black (blue). The spectra have been manually offset.

tronics (4). SWNTs have been slower to find commercial application, but have potential for use as transistors in microelectronics because of their bandgap and as biosensors because of their biomolecular compatibility (4). A carbon nanofiber consists of graphene layers stacked as cones or plates; recently, carbon nanofiber has found applications in construction materials thanks to its flexibility and durability (5).

Because of the intense interest surrounding their unique properties and use in many practical applications, graphene and other graphene-based nanomaterials have now entered the era of large-scale manufacturing. Graphene can be made through various processes including

- mechanical exfoliation, a low-cost technique that involves isolating graphene from bulk graphite (6),
- chemical vapor deposition (CVD), which is performed on a relatively larger scale but at a high cost and with expensive equipment (7,8), and
- exfoliation and reduction of graphene oxide, which is synthesized through the oxidation of graphite

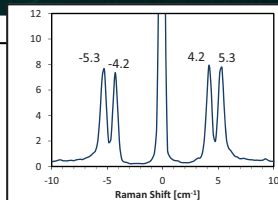
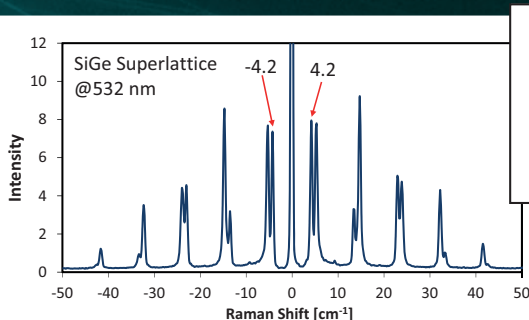
powder on a larger scale, but can result in extensive defects (9).

Although recent market forecasts predict the value of the current global graphene market to be only in the low tens of millions of dollars (10), the value of the global graphene market is estimated to reach half a billion dollars by 2025 (11). It may be decades before the potential of these carbon nanomaterials are fully realized, but research and development spending on graphene is likely to reach hundreds of millions of dollars in the coming years.

To reach these market estimates, one important question for large-scale graphene manufacturing remains: how to easily and rapidly characterize the quality of graphene and other carbon nanomaterials to effectively monitor and control the production process? Raman spectroscopy has been used extensively by carbon nanomaterials research communities in recent years because of its ability to characterize materials from their molecular vibrations (12,13). The Raman spectra of carbon nanomaterials are typically characterized by only three major bands: the

Ultra-Low Frequency Raman Spectroscopy

"Extend your Raman system into THz frequency range ($5\text{-}200\text{ cm}^{-1}$)"



Measured with
LabRAM HR Evolution
(data courtesy of:
HORIBA Jobin Yvon SAS)

BragGrate™ Bandpass and Notch Filters

Spectral and spatial laser line cleaning filters and ultra-narrow line notch filters for low frequency Raman Spectroscopy



Wavelengths
in Production (nm)

405, 442, 458, 473, 488,
491, 514, 532, 552, 561,
568, 588, 594, 632, 660,
785, 830, 980, 1064, 1550

- Frequencies below 10 cm^{-1} with single stage spectrometer
- Angle tunable for precise wavelength adjustment
- Stokes and anti-Stokes Raman bands
- Unlimited optical life-time
- Custom wavelengths in range 400–2000 nm

OptiGRATE
HIGH EFFICIENCY FOR HIGH POWER

+1 (407) 542-7704
info@optigrate.com
www.optigrate.com

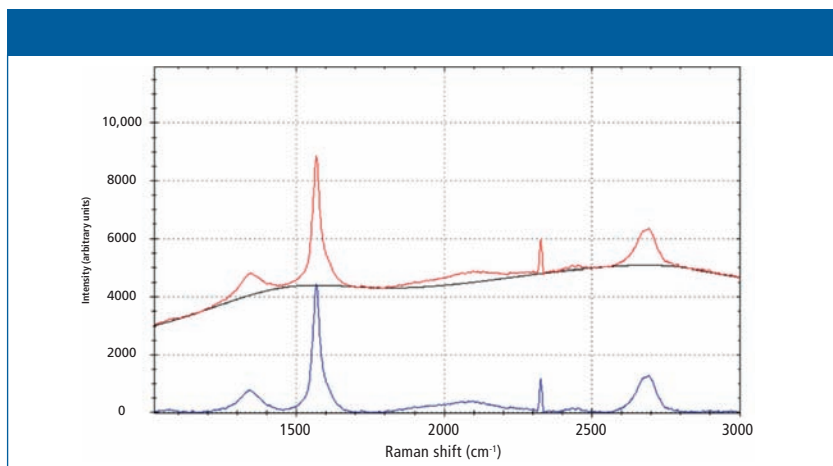


Figure 2: Raman spectrum before (red trace) and after (blue trace) airPLS baseline correction.

G band, the D band, and the 2D band (also known as the G' band). Though simple, the spectra of these nanomaterials are rich in information about their quality and their microstructures as revealed by the peak positions, peak shapes, and peak intensities. The G band appears around 1582 cm^{-1} and represents the graphene in-plane sp^2 vibrational mode (13,14); it is an indication of the crystallinity of the material. The dispersion of the G band can be observed in disordered graphene materials, and the dispersion is proportional to the degree of disorder (15). The D band at around 1350 cm^{-1} is attributed to the structural disorder near the edge of the microcrystalline structure that decreases the symmetry of the structure (14). The Raman peak intensity ratio of these two bands, I_D/I_G , can be used to characterize the degree of disorder of the materials (15). The 2D band appears around 2700 cm^{-1} depending on the laser excitation wavelength and is related to the number of graphene layers (3).

The Raman spectra of monolayer graphene (red), carbon nanotubes (black), single crystal graphite (green),

and carbon black powder (blue) are shown in Figure 1. High-quality graphene is characterized by the sharp, symmetric single peak of the 2D band. The graphite spectrum displays a high amount of order and thus crystallinity characterized by its prominent G band and the absence of a D band. Since graphite is composed of many layers of monolayer graphene, the 2D band observed in the graphite spectrum is much broader and asymmetric than the graphene 2D band, indicating multiple components from several phonon modes. Carbon nanotubes display unique features of the G band. Because of the confinement and curvature of graphene layers in forming nanotubes, the G band becomes asymmetric for MWNT and more likely splits into two bands, the G+ and the G band for SWNT (15). The spectrum of carbon black, which has the lowest amount of crystallinity, displays a strong D band, a broad G band, and a high I_D/I_G ratio, indicating a disordered structure.

Raman spectroscopy provides rich information about the characteristics of

ANY WHERE, ANY TIME, ANALYZE MATERIALS WITH TSI

Laboratory-grade measurement solutions

High performance and easy-to-use Raman spectrometers from TSI meet your needs for affordability, high sensitivity, fast material identification and quantification with short sample times.

The right solution for your application:

- + Handheld Raman Analyzers
- + Benchtop Raman Spectrometers
- + Portable Raman Instruments
- + New direct control with Spectragryph Software



Chem Logix™

For more information visit
tsi.com/molecular-analyzers

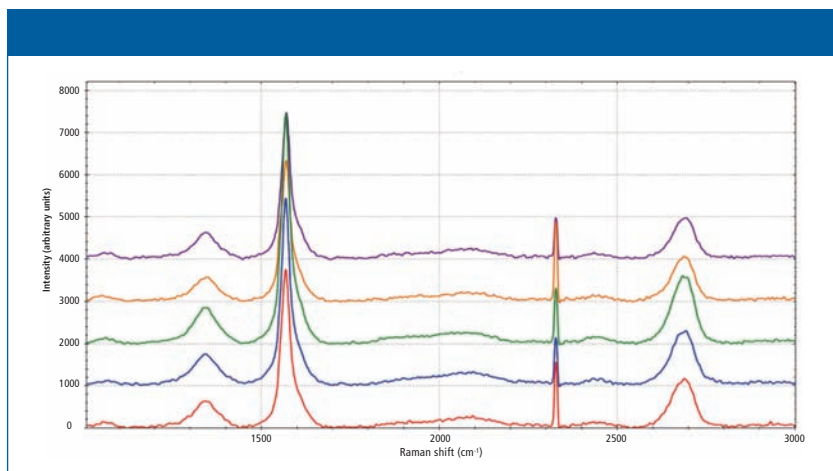


Figure 3: Raman spectra of five locations on a graphene sample. The spectra have been manually offset by 1000 intensity units.

carbon black, graphite, graphene, and other carbon nanomaterials. Although confocal Raman microscopy can provide high-resolution characterization of carbon nanomaterials, the high cost of this instrumentation coupled with the complexity in operation and data interpretation is inadequate for monitoring in a large-scale manufacturing setting, where simple and rapid analytical tools are required. In this study, a high-throughput portable Raman spectrometer is used to characterize three types of materials: graphene powders, carbon nanofibers, and carbon black. This quick analysis can be applied as an at-line or online technique for graphene and other carbon nanomaterials manufacturers to perform materials characterization, product quality control, and process monitoring.

Experimental

An i-Raman Pro HT system (B&W Tek) with a laser excitation of 532 nm via a fiber-optic sampling probe (spot size $\sim 100 \mu\text{m}$) was used for measure-

ments of all samples. The system uses a high-throughput Raman spectrometer with a back-thinned charged-coupled device (CCD) thermoelectrically cooled to -25°C . For materials in powdered forms, no microscope was used. A probe holder with an adjustable xyz stage was used to support the fiber-optic probe over an aluminum pan containing a given carbon sample. The z -focus was used to optimize the working distance from the probe to the sample. BWSpec acquisition software was used for data collection, spectral processing, and programming the automatic calculation of peak intensities and ratios for online measurements or off-line batch processing.

Three types of carbon nanomaterials were analyzed: graphene powders, carbon nanofibers, and carbon black powders. For graphene powders, a laser power of 40 mW with an integration time of 60 s was used to acquire Raman spectra. For carbon nanofiber and carbon black powder samples, an integration time of 90 s was used with a laser power of ~ 21 mW.



Anton Paar



BE FLEXIBLE WITH ANTON PAAR'S RAMAN SPECTROMETERS

- The Cora series of Raman spectrometers provides high resolution on a small footprint
- Multiple wavelengths: Single or dual band for all kinds of samples like fluorescence materials
- Versatile: Suitable for a wide range of solid, semi-solid, or liquid samples
- For quick quality control, identification, qualitative-, and semi-quantitative measurements

Get in touch: www.anton-paar.com

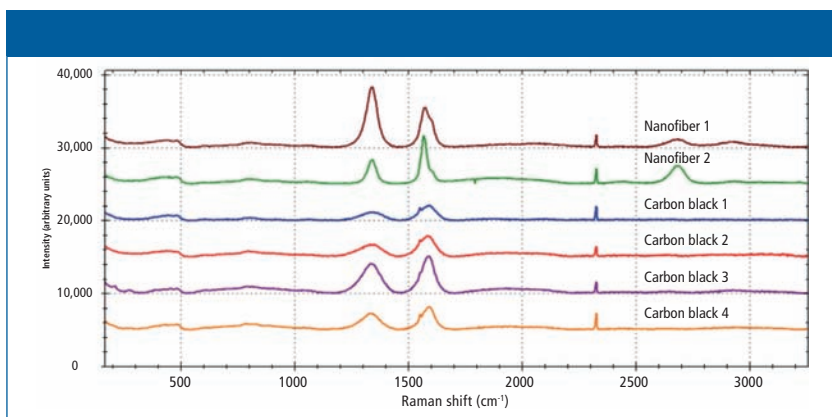


Figure 4: Raman spectra of two carbon nanofiber samples and four carbon black samples. The spectra have been manually offset by 5000 intensity units for clarification.

Three spectra were collected for each sample. No spectral averaging was used.

Results and Discussion

Graphene Powders

Using the adjustable x, y sample stage of the probe holder, 15 measurements from different locations of one graphene powder were collected to assess the uniformity of the sample. Two types of pre-processing were applied to the spectra prior to the peak ratio calculation. First, an adaptive iteratively reweighted penalized least squares (airPLS) background correction was used to remove any fluorescent background present in the spectra. Figure 2 shows an example of before (red trace) and after (blue trace) baseline correction. A Savitzky-Golay smoothing algorithm with a window size of 7 was also applied to all spectra. Figure 3 shows five manually offset representative spectra from different areas of the graphene powder sample. The D band (1346 cm^{-1}), G band (1569 cm^{-1}), and 2D band (2689 cm^{-1}) can be observed. A prominent band at 2328 cm^{-1} is the Q-branch Raman peak for atmospheric nitrogen (N_2) because of the nitrogen-

nitrogen bond (16). The N_2 Raman peak is observed because of the high-throughput nature of the Raman spectrometer.

The ratio I_D/I_G is an important parameter in assessing the level of disorder in the crystal structure of a sample. Table I presents the calculated peak intensities after background removal and intensity ratios for the D and G bands of the five representative spectra. The I_D/I_G ratios of the 15 measurements ranged from 0.1246 to 0.1462. The average I_D/I_G of all 15 scans was 0.1386, with a percent relative standard deviation (%RSD) of 4.07%. This result indicates a high level of uniformity within the sample.

Carbon Nanofibers and Carbon Black

Two carbon nanofiber samples and four carbon black samples were also tested. Three spectra were collected at different locations for each sample. For all collected spectra, an airPLS background correction was used to remove any fluorescent background present in the spectra. A Savitzky-Golay smoothing algorithm with a window size of 5 was also applied to all spectra. Figure 4 shows the manually

Iridian's High Performance Raman Filters

for your Raman and Spectroscopic Applications

Band-pass Filters

- Pass band > 90% transmittance
- Narrow bandwidth; as low as 1 nm
- Blocking (OD>5) from 300 nm to 1200 nm
- Multiple band-pass filters in the UV-VIS-IR region available

Edge Filters

- Pass band > 93% transmittance
- Cut-off values 25-100 cm⁻¹
- Deep Blocking (OD>6)

Wide Angle Ultra-Steep Edge Filters

- Pass band > 90% transmittance
- AOI 0-2 degree; cone half angle
- (CHA) 5 degree
- Cut-off values 0.5% of the wavelength (63.5-93.5 cm⁻¹)
- Deep Blocking (OD>6)

Dichroic Filters

- Pass band > 90% transmittance
- High reflection > 95%
- Tunable AOI 40-50 degree available

Notch Filters

- Pass band > 90% transmittance
- Narrow notch width as low as 10nm
- at 50% width
- Deep Blocking (OD>6)
- Multiple notch available

www.iridian.ca



IRIDIAN
SPECTRAL TECHNOLOGIES



sales@iridian.ca
[@IridianSpectral](https://twitter.com/IridianSpectral)

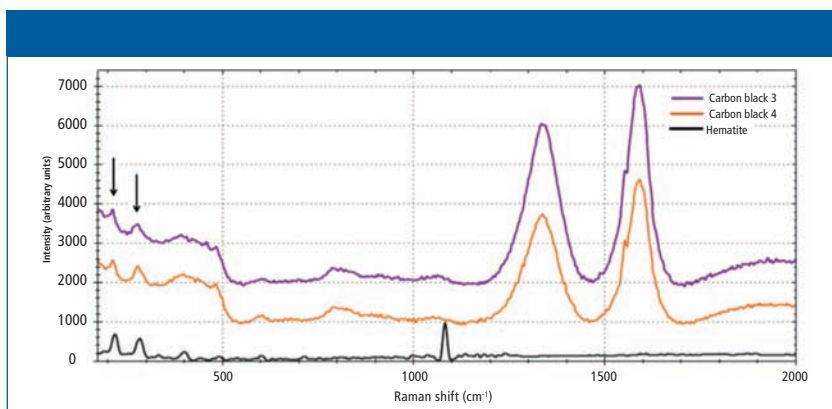


Figure 5: Raman spectra of carbon black 3 (purple) and carbon black 4 (orange). Raman peaks at 213 cm^{-1} and 278 cm^{-1} are consistent with a hematite Raman spectrum (black). The spectra have been manually offset by 1000 cm^{-1} for clarification.

Table I: Calculation of the D-band height, G-band height, and I_D/I_G for five spots in a graphene powder sample

Location	I_D	I_G	I_D/I_G
1	562.1866	4162.1922	0.1351
2	515.6962	3527.9378	0.1462
3	648.8005	5207.1859	0.1246
4	448.6542	3122.5289	0.1437
5	462.5746	3304.4020	0.1400

offset representative spectra for each sample. The four carbon black samples display typical carbon black Raman signatures that contain D and G bands but no 2D band. The two carbon nanofiber samples show prominent D bands, indicating a high level of disorder. The G bands in the carbon nanofiber spectra also exhibit some asymmetry. The asymmetry is likely because of the curvature of the nanofiber, with the slight splitting of the G band induced by curvature of graphene layers when forming the nanofiber (15).

Table II: Average calculated peak intensity ratios for the D band and the G band in carbon black and carbon nanofiber samples

Material Type	Average I_D/I_G ($n = 3$)
Carbon nanofiber 1	1.3654
Carbon nanofiber 2	0.4706
Carbon black 1	0.7667
Carbon black 2	0.7294
Carbon black 3	0.5557
Carbon black 4	0.5745

BWSpec software was used to automatically calculate the I_D/I_G values as spectra were collected. Table II presents the calculated I_D/I_G peak intensity ratios measured for the four carbon black samples and two carbon nanofiber samples. The carbon nanofiber sample 2 has the highest level of order of all samples with an average I_D/I_G of 0.4706, whereas the carbon nanofiber sample 1 has an especially high level of disorder with an average I_D/I_G of 1.3654.

Raman spectroscopy can also be very useful for identifying contami-

nants or starting materials in carbon nanomaterial final products. For example, the carbon black 3 and carbon black 4 samples contain up to 10% hematite (Fe_2O_3) because of their manufacturing processes. Figure 5 shows the Raman spectra of carbon black 3 and 4 compared to the Raman spectrum of hematite. Raman peaks at 213 cm^{-1} and 278 cm^{-1} are in good agreement with the Raman spectrum of hematite.

Conclusions

Having robust and simple quality control tools for carbon nanomaterials such as portable Raman spectroscopy will help facilitate the future growth of the global graphene market. Although simple, a Raman spectrum of a carbon nanomaterial can provide a vast amount of information to characterize materials including carbon black, graphite, carbon nanotubes, and graphene. Portable Raman spectroscopy is capable of quickly characterizing carbon nanomaterials, revealing critical information regarding material qualities such as sample crystallinity and level of disorder using various parameters such as D- and G-band intensity ratios. Graphene manufacturers can easily use the analysis to obtain at-line or online measurements for material characterization, product quality control, and process monitoring.

References

- (1) C. Ahn, S.W. Fong, Y. Kim, S. Lee, A. Sood, C.M. Neumann, M. Asheghi, K.E. Goodson, E. Pop, and H.S.P. Wong, *Nano Lett.* **15**, 6809–6814 (2015).
- (2) H. Hegab and L. Zou, *J. Membr. Sci.* **484**, 95–106 (2015).
- (3) C. Luo, H. Xie, Q. Wang, G. Luo, and C. Liu, *J. Nanomater.* **2015**, 1–10 (2015).
- (4) M.F.L. DeVolder, S.H. Tawfik, R.H. Baughman, and J. Hart, *Science* **339**, 535–539 (2013).
- (5) Y.L. Mo and R.H. Roberts in *Advances in Nanofibers*, R. Maguire, Ed. (InTech, 2013).
- (6) M. Yi and Z. Shen, *J. Mater. Chem. A*. **3**, 11700–11715 (2015).
- (7) C. Mattevi, H. Kim, and M. Chhowalla, *J. Mater. Chem.* **21**, 3324–3334 (2011).
- (8) Y. Zhang, L. Zhang, and C. Zhou, *Acc. Chem. Res.* **46**, 2329–2339 (2013).
- (9) S. Stankovich, D.A. Dikin, R.D. Piner, K.A. Kohlhaas, A. Kleinhammes, Y. Jia, Y. Wu, S.T. Nguyen, and R.S. Ruoff, *Carbon* **45**, 1558–1565 (2007).
- (10) Deloitte Global analysis, 2015, www.deloitte.com/TMTpredictions.
- (11) <https://www.grandviewresearch.com/industry-analysis/graphene-industry>.
- (12) M.S. Dresselhaus, A. Jorio, M. Hofmann, G. Dresselhaus, and R. Saito, *Nano Lett.* **10**, 751–758 (2010).
- (13) A.C. Ferrari and D.M. Basko, *Nat. Nanotechnol.* **8**, 235–246 (2013).
- (14) A.C. Ferrari, J.C. Meyer, V. Scardaci, C. Casiraghi, M. Lazzeri, F. Mauri, S. Piscanec, D. Jiang, K.S. Novoselov, S. Roth, and A.K. Geim, *Phys. Rev. Lett.* **97**, 1874011–1874014 (2006).
- (15) A.C. Ferrari, *Solid State Commun.* **143**, 47–57 (2007).
- (16) D. Tuschel, *Spectroscopy* **29**, 14–21 (2014).

Dawn Yang and Kristen Frano are with B&W Tek in Newark, Delaware. Direct correspondence to: kristenf@bwtek.com or dawny@bwtek.com ■

For more information on this topic, please visit our homepage at: www.spectroscopyonline.com

Gaining Insight into Cocoa Butter Polymorph Formation Through In Situ Rheology and Raman Spectroscopy

Rheology coupled with in situ Raman spectroscopy (rheoRaman) was used to examine the isothermal crystallization of cocoa butter. Two unique isolation protocols were used to form cocoa butter polymorphs form III and form IV. The hyphenation of these two independent analytical techniques, rheology and Raman spectroscopy, enabled a more holistic depiction of the crystallization process and provided unique insights into the formation of cocoa butter polymorphs.

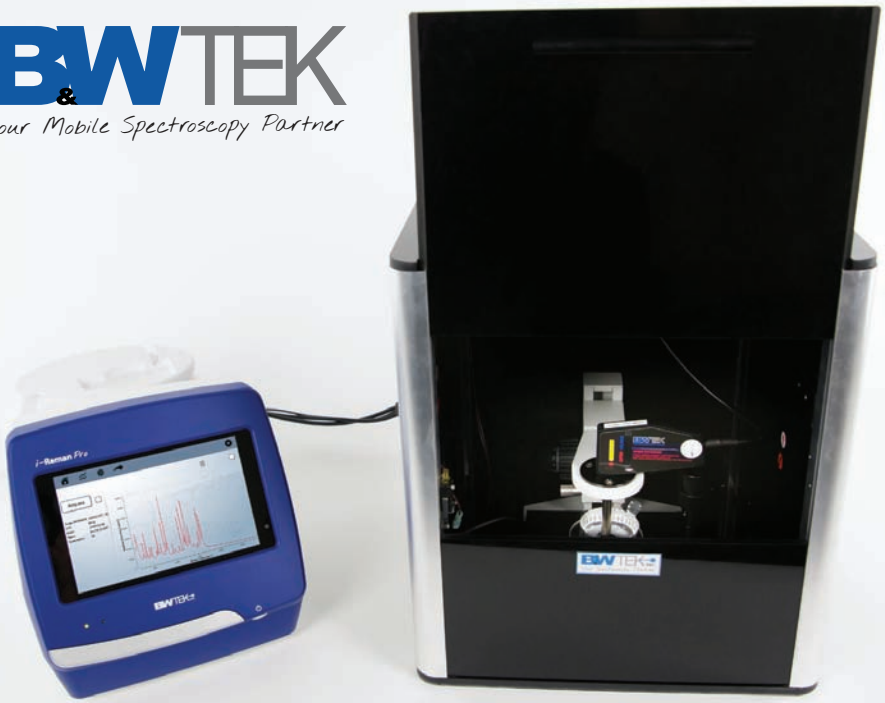
Nathan C. Crawford, Mohammed Ibrahim, and Rui Chen

Cocoa butter is an edible vegetable fat extracted from the cocoa bean. Cocoa butter is commonly used in home and personal care products (such as ointments and lotions) and it is a vital ingredient in chocolate. Cocoa butter forms the continuous phase within chocolate confections and is responsible for the chocolate's texture, snap, gloss, melting behavior, and resistance to fat bloom. These physical characteristics are a direct result of cocoa butter's triacylglycerol (TAG) composition and overall crystalline structure.

In general, TAG molecules assume a tuning fork configuration and the TAG "forks" assemble to form crystal lattice structures. During crystallization, the TAG molecules slow down as the cocoa butter oil cools and the TAGs come to rest in contact with one an-

other, forming subcrystalline cells (1). After the subcells are formed, they are thermodynamically driven to aggregate into larger and more-stable crystalline structures (2). The self-assembly of subcell structures and their further aggregation is governed by a balance of intra- and intermolecular interactions. Depending on the molecular level packing and orientation of the TAGs, cocoa butter can form different types of crystal lattice structures, commonly referred to as *polymorphs*.

Researchers have identified six unique cocoa butter polymorphs (3)—form I, II, III, IV, V, and VI—each with a distinct molecular signature. Form V is the polymorph most commonly found in commercially available chocolates, and it is believed that all other polymorphs lead to inadequate properties or a shortened shelf life. For



All New Portable Carbon Raman Analyzer

B&W Tek's Carbon Raman Analyzer (CRA) is a portable Raman system with 532nm laser excitation and a fiber optic sampling probe. It is ideal for materials in powdered forms, with no need for sample preparation or microscope.

Learn More About the Carbon Raman Analyzer
www.bwtek.com/CRA

example, form IV is often associated with poorly or under-tempered chocolate; whereas form VI is considered to cause fat bloom, the greyish surface coating sometimes observed on old or temperature-abused chocolate. As a result, the chocolate tempering process is critical because it ensures that the cocoa butter has assembled into the desired crystalline polymorph.

Overall, cocoa butter crystallization is a highly complex, multistage process. Understanding the isothermal crystallization behavior of cocoa butter is vital for improving chocolate manufacturing processes and maintaining product quality. Cocoa butter crystallization has been widely studied using a variety of analytical techniques, including differential scanning calorimetry (DSC), X-ray diffraction (XRD), X-ray scattering, rheology, and Raman spectroscopy (2,4–7). Although cocoa butter crystallization has been thoroughly examined from the molecular, microstructural, and macroscopic levels, a lack of consensus about the existence of some cocoa butter polymorphs, the overall crystallization kinetics (especially in the presence of additives), and the underlying mechanisms of the crystallization process still persist.

In this study, rheology coupled with in situ Raman spectroscopy was used to examine the isothermal crystallization of cocoa butter. Raman spectroscopy is a highly sensitive, relatively fast, and nondestructive technique that can probe the molecular structure and conformation in both liquid and solid TAG assemblies, as well as intra- and inter-TAG interactions. With simultaneous Raman and rheological measurements, molecular-level

interactions and conformational shifts during the isothermal crystallization of cocoa butter were directly correlated with the changes in bulk viscoelastic properties, providing unique insight into the multifaceted crystallization behavior of cocoa butter.

Materials and Methods

Materials

Commercially available, organic cocoa butter (*Theobroma cacao*) was acquired from Inesscents.

Rheology

Rheological measurements were performed using a Thermo Scientific HAAKE MARS 60 rheometer equipped with a serrated 35-mm-diameter plate rotor at a gap height of 1 mm. The serrated plate was used to prevent slip at the sample-rotor interface. All measurements were conducted using oscillatory shear, with a frequency of 1 Hz and a constant strain of 0.1%; data were collected every 10 s. Cocoa butter samples were loaded onto the rheometer at 60 °C and allowed to equilibrate for 10 min to erase any crystal structures or shear history from sample loading. After the equilibrium step, samples were exposed to one of the following temperature ramp and isothermal hold procedures to generate cocoa butter polymorph form III or form IV (2):

Form III (Slow Cooling)

- Temperature decreased from 60 °C to 14 °C at a rate of 2 °C/min
- Temperature held constant at 14 °C for 60 min

Form IV (Rapid Cooling)

- Temperature decreased from 60 °C to 22 °C at a rate of 10 °C/min

Just like riding a bike.



CONFOCAL RAMAN MICROSCOPY

Spectra Manager™ includes an imaging tool for the creation of very clear and sharp Raman mapping images.

The Analysis Wizard™ guides the user through the analysis and imaging process for accurate overlapping of the display colors in a distribution map to make a

clear differentiation between the components or phases in a sample.



The wizard starts with truncation of the region of interest, followed by digital filtering, noise reduction, a combination of artificial intelligence and multivariate curve resolution (MCR) to create the highest quality image maps.

The logo for JASCO, featuring the word "JASCO" in a stylized, green, italicized font.

PERFORMANCE • INNOVATION • RELIABILITY

www.jascoinc.com

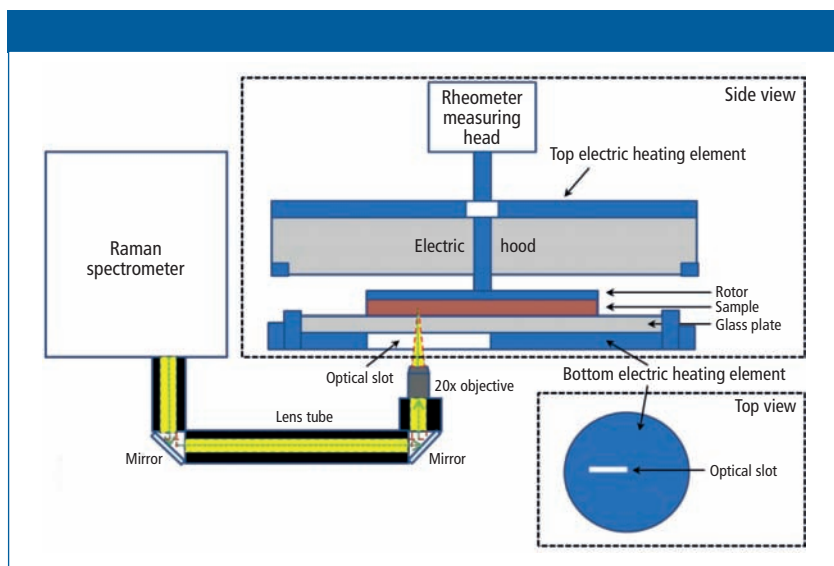


Figure 1: Schematic diagram of the rheoRaman system (MARS_{xR}) showing side and top views of the rheometer sample stage. The iXR Raman spectrometer is free-space coupled to the MARS rheometer using lens tubes and mirrors that direct light into a 20x objective. The objective focuses the incoming laser (green dashed line) and collects the back-scattered Raman light (yellow) coming out of the sample sitting atop the rheometer stage.

- Temperature held constant at 22 °C for 120 min

The melt-to-solid phase transition of cocoa butter was probed rheologically using small amplitude oscillatory shear measurements, where the storage modulus G' and loss modulus G'' were measured as a function of time. The overall magnitudes of G' and G'' , as well as the ratio of $G''/G' = \tan(\delta)$, determine the general viscoelasticity and overall resistance to deformation for a given material. The term “ $\tan(\delta)$ ” is also referred to as the loss or damping factor where δ is the phase angle defined as the shift or lag between the input strain and resultant stress sine waves (or vice versa) during an oscillatory shear measurement. Values of $\tan(\delta)$ less than unity indicate elastically dominant (solid-like) behavior,

whereas values greater than unity indicate viscously dominant (liquid-like) behavior. Unlike the individual moduli, $\tan(\delta)$ can be used to quantify overall brittleness of a material and is commonly used to assess glass transition behavior. In general, as $\tan(\delta)$ becomes smaller, the more G' deviates from G'' , and the more brittle (or glass-like) the material becomes.

Raman Spectroscopy

Raman spectroscopy measurements were performed using a Thermo Scientific iXR Raman spectrometer. The iXR system used a 532-nm laser operated at 10-mW power at the sample. Data acquisition and processing were carried out using the Thermo Scientific OMNIC for Dispersive Raman software. Sequential Raman spectra

Life saving decision making in the palm of your hand!



Mira DS is the new handheld material identification system from Metrohm. Identify hazardous materials and explosives in seconds!



- **Powerful** – respond to threats faster and safer than ever
- **Fast** – get actionable intelligence in seconds
- **Flexible** – be prepared for every treacherous situation
- **Rugged** – MIL-STD-810G and IP67 certified

Watch a demo on metrohm.com/mira-ds

 Metrohm

75 YEARS
PEOPLE YOU CAN TRUST

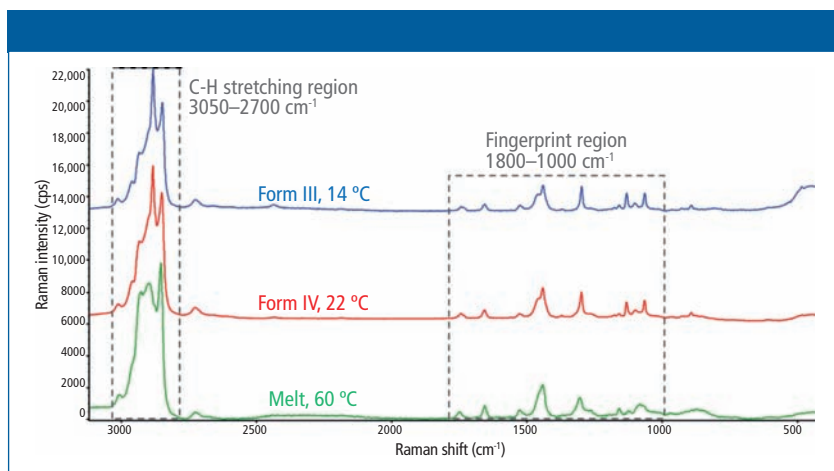


Figure 2: The full Raman spectra for the melt phase and two polymorphs (forms III and IV) of cocoa butter.

(in parallel with the rheological measurements) were collected over a pre-determined time window using the time series collection function of the SERIES software within the OMNIC for Dispersive Raman package. Spectra were collected as an average of four 2-s sample exposures.

RheoRaman Coupling

The Raman spectrometer (Thermo Scientific iXR Raman spectrometer) and rheometer (Thermo Scientific HAAKE MARS 60) were coupled together using the Thermo Scientific HAAKE rheoRaman module. The iXR Raman spectrometer was free-space coupled to the rheometer with an optical train that used a series of mirrors to direct the incident laser into the rheoRaman module (Figure 1).

The sample was positioned between a sandblasted glass bottom plate and the serrated 35-mm plate rotor to avoid slippage at the sample–plate interfaces. An electrical heating element within the rheoRaman module pro-

vided temperature control from below the sample, while an active electrical hood was used to provide temperature control from above (eliminating the potential for a temperature gradient within the sample). Cooling of the sample was supplied from a temperature-controlled water bath circulator.

Results and Discussion

Cocoa Butter Raman Spectroscopy

Full range (500–3100 cm⁻¹) Raman spectra for the liquid-phase cocoa butter and the two investigated solid phase cocoa butter polymorphs (forms III and IV) are shown in Figure 2. Prominent Raman features were observed in both the C–H stretching region (2700–3050 cm⁻¹) and the fingerprint region (1000–1800 cm⁻¹). More specifically, the lower Raman shift features include the carbonyl (C=O) stretching region (1700–1800 cm⁻¹), the olefinic (C=C) band at ~1655 cm⁻¹, the CH₃ and CH₂ deformations (~1460 and 1440 cm⁻¹, respectively), the CH₂ twisting re-

Next generation Raman imaging



High performance Raman systems for a range of applications

Raman spectroscopy produces chemical and structural images to help you understand more about the material being analysed. You can determine:

- if a specific material or species is present
- if any unknown materials are present in the sample
- the variation in a parameter of a material, such as crystallinity or stress state
- the distribution of the material or species
- the size of any particles or domains
- the thickness and composition of layered materials, such as polymer laminates, from micrometres to millimetres thick
- the relative amounts of materials or species

Renishaw has decades of experience developing flexible Raman systems that give reliable results, even for the most challenging measurements.

With Renishaw's suite of Raman systems, you can see the small things, the large things and things you didn't even know were there.

Visit www.renishaw.com/raman

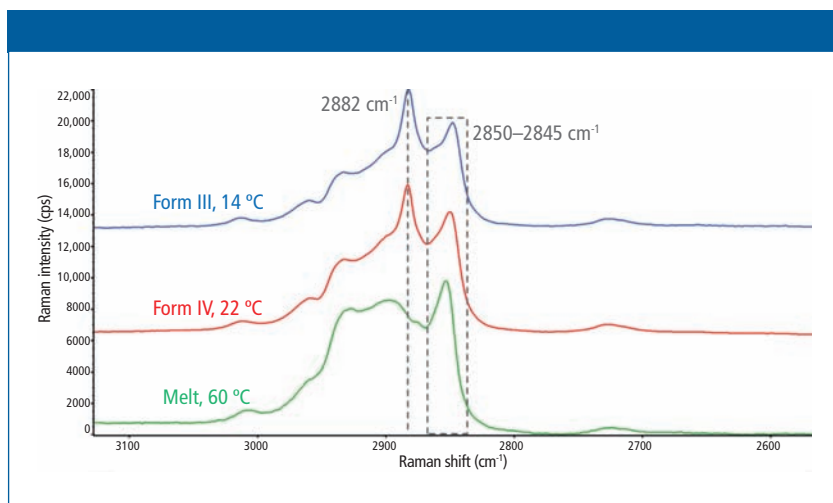


Figure 3: Raman spectra of the C-H stretching region ($2700\text{--}3050\text{ cm}^{-1}$) for the melt phase and two polymorphs (forms III and IV) of cocoa butter.

gion ($1250\text{--}1300\text{ cm}^{-1}$), and the C-C stretching region ($1000\text{--}1200\text{ cm}^{-1}$).

The C-H stretching regions for the melted and solidified cocoa butter specimens are highlighted in Figure 3. Two strong peaks were observed at $\sim 2850\text{ cm}^{-1}$ and 2882 cm^{-1} , which are attributed to symmetric and asymmetric CH_2 stretching, respectively (2). The symmetric vibrational modes at 2850 cm^{-1} were dominant in the liquid (melt) phase, indicating reduced lateral interactions between CH_2 groups and a low degree of intermolecular interactions. Conversely, the asymmetric vibrations at 2882 cm^{-1} were dominant in the solid phase, which suggests increased lateral interactions resulting from closely packed crystalline structures. Thus, the 2850 cm^{-1} and 2882 cm^{-1} bands are strong indicators of amorphous and crystalline content, respectively (8). Subsequently, the I_{2882}/I_{2850} peak intensity ratio was used to dynamically track

crystal formation during the in situ rheoRaman measurements.

Although they are less intense than the C-H stretching region, approximately eight unique spectral features were identified in the fingerprint region ($1000\text{--}1800\text{ cm}^{-1}$; Figure 4). When comparing the cocoa butter melt state to the crystalline cocoa butter polymorphs, the most significant changes were observed in the C-C stretching region ($1000\text{--}1200\text{ cm}^{-1}$). Two well-defined features emerged at 1130 cm^{-1} and 1063 cm^{-1} during the solidification process, which originate from the symmetric and asymmetric C-C stretching, respectively (9,10). In the melt phase, all C-C stretching bands were relatively weak and broad because of the disordering effects of methyl gauche conformations. However, as the cocoa butter solidified, the backbone methyl groups were ordered into the trans conformation, signified by the emergence of the peak at 1130 cm^{-1} . Therefore, in addition to

SEE THE WHOLE PICTURE

The new
Morphologi 4-ID

Award-winning
design

ADVANCED PARTICLE CHARACTERIZATION USING MORPHOLOGICALLY-DIRECTED RAMAN SPECTROSCOPY (MDRS)

- Combines static automated imaging and Raman spectrometry for rapid, component-specific morphological characterization
- Solves formulation and deformation challenges
- Helps control and optimize processes and products
- Creates confidence and clarity throughout development and manufacturing, quickly identifying issues and changes



www.malvernpanalytical.com/morphologi

 **Malvern
Panalytical**
a spectris company

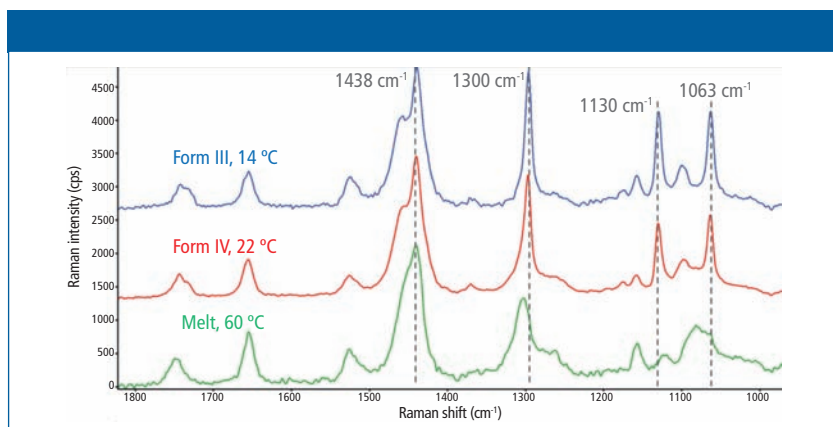


Figure 4: The 1000–1800 cm^{-1} Raman spectral range for the melt phase and two polymorphs (forms III and IV) of cocoa butter.

the I_{2882}/I_{2850} peak intensity ratio, the I_{1130}/I_{2850} spectral marker was also used to track the crystalline-phase transition within cocoa butter via in situ rheoRaman measurements.

Form III: Simultaneous Rheology and Raman Spectroscopy

To form cocoa butter polymorph form III, the temperature was ramped down from 60 °C to 14 °C at a rate of 2 °C/min. During cooling and before reaching the isothermal temperature of 14 °C, both the elastic and viscous moduli (G' and G'' , respectively) began to increase exponentially at ~20 min and ~20 °C (Figure 5a). From 20 to 25 min, as the temperature was further decreased and then held at 14 °C, G' and G'' increased by approximately six and five orders of magnitude, respectively. The rapid increase in the moduli indicates the start of the solidification process, where the cocoa butter specimen transformed from a semisolid material into a firm solid. After the temperature reached the constant value of 14 °C, the elastic modulus began to plateau at 30 min,

whereas the viscous modulus reached a maximum at ~25 min and then gradually decreased from ~25 to 55 min. From 55 min and beyond, both G' and G'' remained constant. After 55 min, G' was about two orders of magnitude greater than G'' , suggesting that the cocoa butter was now a rigid, glass-like solid. From a purely rheological standpoint, the cocoa butter appeared to have fully crystallized.

The rheological measurements for cocoa butter form III were further corroborated using in situ Raman spectroscopy (Figure 5b). Similarly to G' and G'' , both the I_{1130}/I_{2850} and I_{2882}/I_{2850} peak intensity ratios remained relatively constant during the first ~20 min of the measurement. Then the I_{1130}/I_{2850} and I_{2882}/I_{2850} spectral markers began to abruptly increase at ~20 min, indicating the formation of crystalline structures within the cocoa butter. As the cocoa butter further crystallized, both spectral ratios continued to increase from 20 to 70 min. After ~70 min, the Raman peak intensity ratios began to stabilize as the cocoa butter TAGs arranged into their final

crystal structure. Significant scatter in the y -direction was observed for the I_{1130}/I_{2850} ratio, especially at the earlier melt state and at the latter part of the crystallization process. This scatter was most likely because of the low intensity of the 1130 cm^{-1} feature in comparison to the strong Raman bands in the C-H stretching region (2850 cm^{-1} and 2882 cm^{-1}).

Notably, the initial increase in G' and G'' directly aligned with the rise of the 1130 and 2882 cm^{-1} spectral ratios. The concurrent increases in both the rheological response and Raman feature intensity suggests that the bulk solidification during the formation of cocoa butter polymorph form III was directly associated with the formation of crystalline structures. Interestingly, as the change in rheological behavior began to subside at 55 min, the Raman spectral features were still increasing and they did not become steady until ~ 70 min and beyond. It is postulated that although the overall bulk hardening of the cocoa butter had stopped, the crystalline domains were still rearranging at the molecular level and that the cocoa butter had not reached its final crystalline lattice structure until the end of the measurement.

Form IV: Simultaneous Rheology and Raman Spectroscopy

To form cocoa butter polymorph form IV, the temperature was rapidly decreased from $60\text{ }^{\circ}\text{C}$ to $22\text{ }^{\circ}\text{C}$ at a rate of $10\text{ }^{\circ}\text{C}/\text{min}$. Note that since the cooling step was so brief, only the data from the isothermal step is shown in Figure 6. During the initial portion of the isothermal hold from 0 to 5 min (immediately following the rapid decrease in temperature from $60\text{ }^{\circ}\text{C}$ to $22\text{ }^{\circ}\text{C}$), both

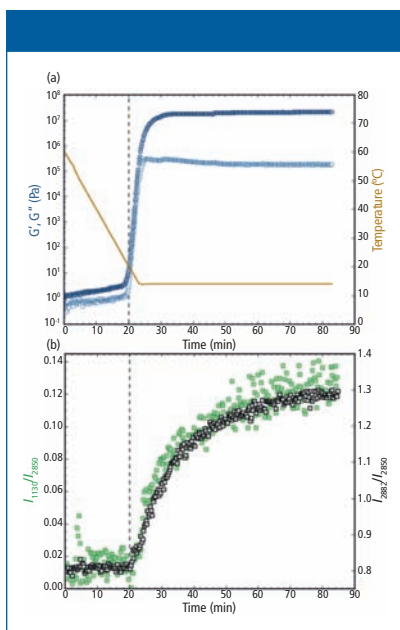


Figure 5: (a) Rheology: G' and G'' (filled and open circles, respectively; plotted on the left y -axis) and the temperature trace (solid line; plotted on the right y -axis) and (b) Raman: the I_{1130}/I_{2850} (left y -axis) and I_{2882}/I_{2850} (right y -axis) intensity ratios for cocoa butter during the melt-crystalline transition to polymorph form III from $60\text{ }^{\circ}\text{C}$ to $14\text{ }^{\circ}\text{C}$. The vertical dashed line at 20 min indicates the increase in both G' and G'' and the Raman intensity ratios.

G' and G'' increased as the cocoa butter transformed from a melted liquid to a soft semisolid (Figure 6a). This initial increase in modulus is most likely because of a delay between the set temperature and the internal temperature of the loaded sample. After the sample had reached thermal equilibrium and was at the isothermal set point of $22\text{ }^{\circ}\text{C}$, the moduli were relatively stable from 10 to 25 min. From 25 to 50 min, however, both G' and G'' began to gradually increase and then from 50 to 80 min, the moduli rapidly in-

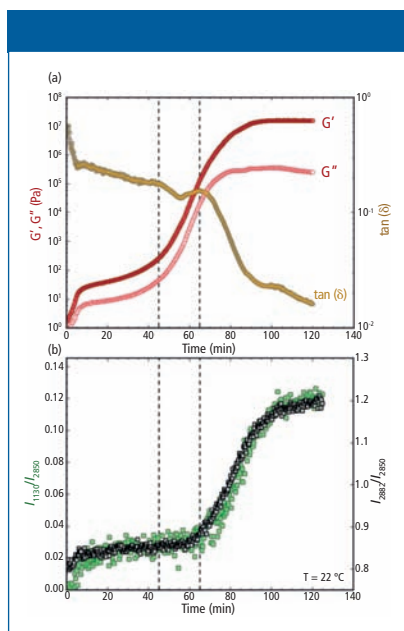


Figure 6: (a) Rheology: G' and G'' (filled and open circles, respectively; plotted on the left y-axis) and $\tan(\delta)$ (plotted on the right y-axis) and (b) Raman: the I_{1130}/I_{2850} (left y-axis) and I_{2882}/I_{2850} (right y-axis) peak intensity ratios for cocoa butter during isothermal crystallization at 22 °C. The vertical dashed line at 45 min indicates the increase of G' and G'' , while the dashed line at 65 min indicates the decrease in $\tan(\delta)$ and increase in the Raman intensity ratios.

creased, where G' and G'' increased by approximately five and four orders of magnitude, respectively. The exponential increase in the moduli indicates a solidification process, where the cocoa butter transformed from a pliable semisolid to a more robust, hardened solid. At 80 min and beyond, growth in the elastic modulus slowed and eventually plateaued, showing no further significant change past 100 min. The viscous modulus, however, reached a slight plateau from 80 to 100 min but

continued to decrease from 100 min and beyond.

During the increase in G' and G'' , a rapid decrease in the loss factor $\tan(\delta)$ was observed from ~ 65 min and beyond (Figure 6a, right y-axis). The decrease in the loss factor indicates a deviation in overall magnitude between G' and G'' . As the cocoa butter hardened, the increase in G' exceeded the increase in G'' , triggering the decrease in $\tan(\delta)$. At the end of the 120 min isothermal study, G' was more than a full order of magnitude greater than G'' and the loss factor was approaching 0.01, indicating the cocoa butter had transitioned into a brittle glass-like solid.

The observed rheological behavior was further confirmed using simultaneous Raman spectroscopy (Figure 6b). Initially, both the I_{1130}/I_{2850} and I_{2882}/I_{2850} peak intensity ratios remained unchanged during the first ~ 65 min of the isothermal study. Then a sharp increase of the I_{1130}/I_{2850} and I_{2882}/I_{2850} ratios began at ~ 65 min, indicating the formation of crystal structures within the cocoa butter. As the cocoa butter further crystallized, both spectral markers continued to increase from 65 to 100 min. Beyond 100 min, the growth in both Raman features had subsided and the peak intensity ratios began to stabilize.

Overall, the rate of increase in the 1130 and 2882 cm^{-1} peak intensity ratios were similar to the rate of change for both G' and G'' during the formation of cocoa butter polymorph form IV (Figures 6a and 6b). However, there was a noticeable 15–20 min lag between the observed increase in G' and G'' and the rise of the Raman intensity ratios. The sharp upturn in G' and G''

indicates an increased resistance to deformation (that is, a bulk hardening of the cocoa butter), signaling the start of the solidification process. The Raman spectral markers, on the other hand, are indicators of crystal formation. Thus, the time delay between the rheology and Raman profiles suggests that cocoa butter first hardens into an amorphous solid, followed by a transformation from an amorphous to a crystalline solid. This morphological transformation was signified by the subsequent increase in the Raman band intensities associated with crystal cocoa butter structures (the 1130 and 2882 cm^{-1} peaks). The temporal separation of the rheological and Raman spectral profiles indicates a clear distinction between bulk hardening of the cocoa butter and the formation of crystalline domains during the formation of polymorph form IV.

Interestingly, the increase in the Raman spectral features (I_{1130}/I_{2850} and I_{2882}/I_{2850}) directly correlated with the observed reduction in $\tan(\delta)$ (Figures 6a and 6b). The loss factor is an indication of material brittleness and crystalline structures are commonly known to be brittle. Thus, it is reasonable to infer that the formation of crystal domains at the molecular level (as indicated by Raman) coincides with the overall brittleness of the cocoa butter. As a result, the loss factor may be a more revealing indicator of bulk cocoa butter crystallization than G' and G'' alone.

Conclusions

Simultaneous rheology and Raman spectroscopy measurements were used to examine the isothermal crystallization of cocoa butter. This multimodal analytical technique allowed the bulk

mechanical properties of cocoa butter (G' , G'' , and $\tan[\delta]$) to be directly correlated with conformational changes at the molecular level ($\nu_{\text{as}}[\text{CH}_2]$ mode at 2882 cm^{-1} and the $\nu_{\text{s}}[\text{C-C}]$ mode at 1130 cm^{-1}) in real-time. With a slow cooling (2 $^{\circ}\text{C}/\text{min}$) and subsequent isothermal hold at 14 $^{\circ}\text{C}$, the concurrent increases in both the rheological response and Raman feature intensity suggests that the bulk solidification during the formation of cocoa butter polymorph form III coincided with the formation of crystalline structures. With a rapid cooling (10 $^{\circ}\text{C}/\text{min}$) followed by an isothermal hold at 22 $^{\circ}\text{C}$, however, there was a noticeable time lag between the rheological response (G' and G'') and the Raman spectral profiles during the formation of cocoa butter polymorph form IV. The observed time delay indicates that cocoa butter crystallized by first hardening into an amorphous solid, manifested by a sharp increase in G' and G'' while the Raman features remained unchanged. The amorphous solid then underwent a morphological transition to form a crystalline solid, signified by the increase in Raman features associated with crystal cocoa butter structures (1130 and 2882 cm^{-1}). Without coupling these two separate analytical techniques, the observed amorphous-solid to crystalline-solid transformation would have been left undetected. Alone, each technique suggests a single stage process, however, only when the two techniques are coupled is the multiphase crystallization process revealed, further exemplifying the unique analytical capability unleashed by hyphenating rheology with in situ Raman spectroscopy.

Continued on page 49

Data-Driven Raman Spectroscopy in Oil and Gas: Rapid Online Analysis of Complex Gas Mixtures

Gas analysis systems used for mud logging in the oil and gas industry provide information that is critical to optimize the drilling process and for ensuring safety on-site. As drilling speeds increase, measurement of hydrocarbons and nonhydrocarbons in real time becomes more challenging for traditional methods like gas chromatography (GC). Raman spectroscopy offers a promising alternative for multicomponent analysis of complex gas mixtures, particularly when high-sensitivity compact Raman instrumentation is combined with advanced data analysis. Here we share a new data-driven Raman spectroscopy (DDRS) method capable of simultaneously measuring 12 hydrocarbon and nonhydrocarbon gases in the presence of matrix interferences. Validation of its performance using both standard gas mixtures and two real mud-logging data sets compared favorably against the GC method, demonstrating the feasibility of this technique for online, high-throughput quantitative analysis of gases in oil and gas exploration and recovery, as well as many other industries.

Da Chen and Cicely Rathmell

A *mud log* details the composition and characteristics of the rock cuttings, mud, and gases brought to the surface by borehole drilling during oil and natural gas exploration. It provides valuable information about the quality and status of a drill site, logging the position and mix of hydrocarbons to facilitate efficient extraction and provide advance warning of dangerous gas levels (1). As rocks are crushed

in the drilling process, a variety of gases indicative of the reservoir are released, including hydrocarbons such as methane, ethane, propane, isobutane, normal butane, isopentane, and normal pentane as well as a variety of nonhydrocarbons: CO₂, CO, O₂, N₂, and H₂. Rapid, continuous analysis of the composition of these complex mixtures is essential to help workers respond quickly to changes during drilling.

Gas Chromatography Versus Raman Spectroscopy

Although gas chromatography (GC) is the most widely used technique for the evaluation of multicomponent gases (2), it is limited both in speed (3) and its ability to distinguish between hydrocarbons and nonhydrocarbons simultaneously. GC also carries on-going costs in the form of consumable columns, associated maintenance, and the need for trained operators.

Raman spectroscopy, in contrast, can be performed in just seconds, requires no sample preparation, and does not consume the sample. It has very little sensitivity to water vapor, and can probe all the relevant hydrocarbon and nonhydrocarbon gases concurrently. The challenge in making this technique widely deployable lies in achieving the sensitivity and specificity required to quantify each component within the complex, widely varying gas mixtures extracted from boreholes.

Since the first application of Raman spectroscopy to natural gas detection in 1980 (4), many variations have been proposed to enhance the signal, with successful deployment in some process analysis and onsite applications. Although specialized techniques can go so far as to achieve sub-parts per million detection limits, if Raman is to replace GC in the industry, the instrumentation must also be compact and portable enough for onsite deployment while still retaining sufficient sensitivity for meaningful quantitative analysis. Improvements in detection efficiency are part of the equation, but systems must also be able to quantify both hydrocarbon and nonhydrocarbon gases within the same matrix in a timely manner.

Analysis Challenges and Proposed Solution

The Raman spectra of complex gas mixtures of the type seen in mud logging are composed of many overlapping bands, and are also subject to considerable matrix interference. Those challenges demand the development of new chemometric analysis methods that are capable of deconvoluting superimposed spectra and neglecting background and matrix effects. The present body of work introduces a new approach called *data driven Raman spectroscopy* (DDRS) (5). DDRS is an application of partial least squares (PLS) analysis that combines higher-density discrete wavelet transform (HDWT) with variable selection influenced by the data itself, with the goal of isolating the most useful spectral features for target gas quantification in complex multicomponent mixtures. Instead of analyzing Raman spectra based on matching individual peaks at discrete wavelengths, DDRS uses an HDWT representation of the Raman spectrum to extract the most relevant spectral bands for the analysis of each given component.

Wavelet Transforms and Raman

A *wavelet transform* breaks down data into its frequency band components, allowing sharp changes in signal to be easily discriminated from noise. This concept has been applied to good effect in JPEG compression of images, which uses two-dimensional (2D) discrete wavelet transform (DWT) to find the local changes in brightness that truly define an image, filtering out noise and allowing the image to be compressed without loss of crucial

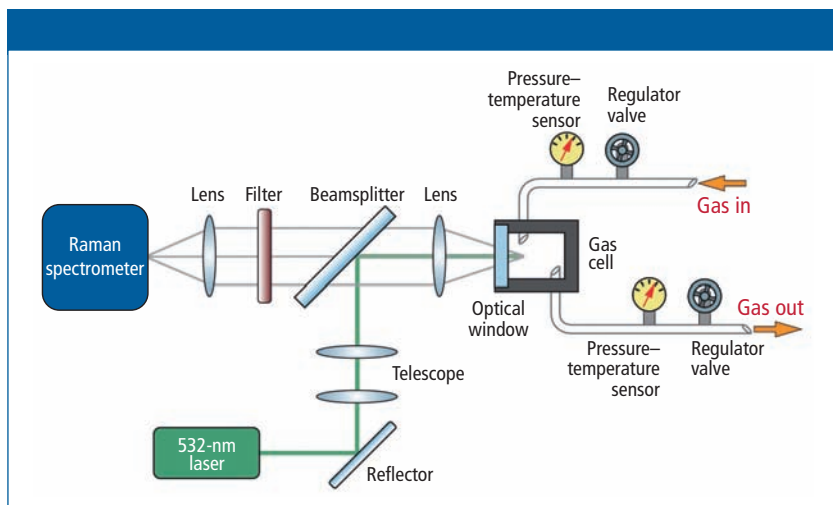


Figure 1: Design of the Raman gas analysis system. A 532-nm laser was coupled into the gas cell for excitation of Raman scattering, with longpass filtering of signal before detection by a high-sensitivity Raman spectrometer.

details. Similarly, DWT has proven useful for background subtraction in Raman spectra (6).

DWT samples data in both the frequency and time domains. In the case of Raman spectra, the frequency domain correlates to peak width, while the time domain correlates to peak position. Raman spectra contain a rich amount of information in the form of both peak position and width, facilitating analysis in the frequency domain (peak width resolution) to mitigate the effects of background and noise, as well as in the time domain (peak wavelength position) to isolate analyte-specific spectral bands from the presence of other species and matrix interference.

Data-Driven Raman Spectroscopy

In developing the DDRS methodology, two key elements of a typical DWT approach were modified to overcome known weaknesses and improve its applicability to the analysis of multicom-

ponent gases. The first improvement related to the transform itself. DWT down-samples data which, in the case of spectra, has the effect of degrading spatial resolution in the time (peak position) domain. To offset this effect, an oversampling technique called *high-density discrete wavelet transform (HDWT)* was used. HDWT was developed to improve both the time and frequency resolution of DWT (7), and to mitigate a known vulnerability of traditional DWT to the alignment of the signal in time (or peak position, in the case of Raman). When applied to overlapping spectral bands in mixtures, the improved spectral resolution of HDWT allowed interfering components to be more easily distinguished. It also has the practical benefit of making the transform less sensitive to wavelength shifts, which is extremely important for Raman instrumentation operating in harsh environments and over a wide range of temperatures.

Table I: Performance of the DDRS model for prediction of 12 gases in the validation set, adapted with permission from reference 5

	Variable Number	PLS Factors	RMSEP	R/A (%)	R	LOD (%)
Methane	13	2	0.0033	3.1	0.999	0.057
Ethane	9	2	0.0075	7.1	0.999	0.024
Propane	9	2	0.0022	2.7	0.999	0.013
Isobutane	12	2	0.0023	11.5	0.994	0.027
Normal butane	16	2	0.0011	6.5	0.996	0.016
Isopentane	10	2	0.0008	11.4	0.983	0.021
Normal pentane	6	2	0.0007	11.7	0.986	0.012
Carbon dioxide	7	2	0.0009	2.6	0.999	0.051
Carbon monoxide	10	2	0.0010	3.0	0.999	0.078
Oxygen	4	2	0.0613	8.8	0.969	0.075
Nitrogen	3	2	0.0045	7.6	0.998	0.065
Hydrogen	4	2	0.0016	3.6	0.999	0.086

The second improvement defining DDRS lies in selection of the variables for PLS analysis—the unique spectral features that will allow each component to be identified and quantified with minimal overlap and greatest accuracy. A random frog algorithm is typically used for this purpose, but because this approach often results in the selection of unimportant variables, a template-oriented frog algorithm (TOFA) was proposed, in which variables are weighted by an estimate of their importance. For a detailed description of the HDWT and TOFA methodology and application, readers are referred to the literature (5).

Together, these two improvements to traditional DWT define a DDRS analysis method intended to isolate the optimal combination of spectral features for each component gas with minimum overlap, and then construct high-quality calibration models for gas analysis. To test its potential for ex-

tracting quantitative information, the method was put through its paces with a series of known multicomponent gas mixtures. It was also compared to GC analysis in continuous monitoring studies at two actual gas logging sites.

Experimental

To be viable for use in oil and gas exploration, a Raman spectroscopy system must be compact, robust, and capable of delivering repeatable data over a wide range of conditions, often harsh. The system built to test the DDRS method (Figure 1) was designed with onsite measurement in mind, integrating a 532-nm, 300-mW diode-pumped solid-state laser (WSLS-532-300 m, Wavespectrum Laser Group Limited) with a high numerical aperture Raman spectrometer for optimum throughput (Wasatch Photonics 532 Raman spectrometer, $f/1.3$). The spectrometer utilized a 1624-lines/mm volume

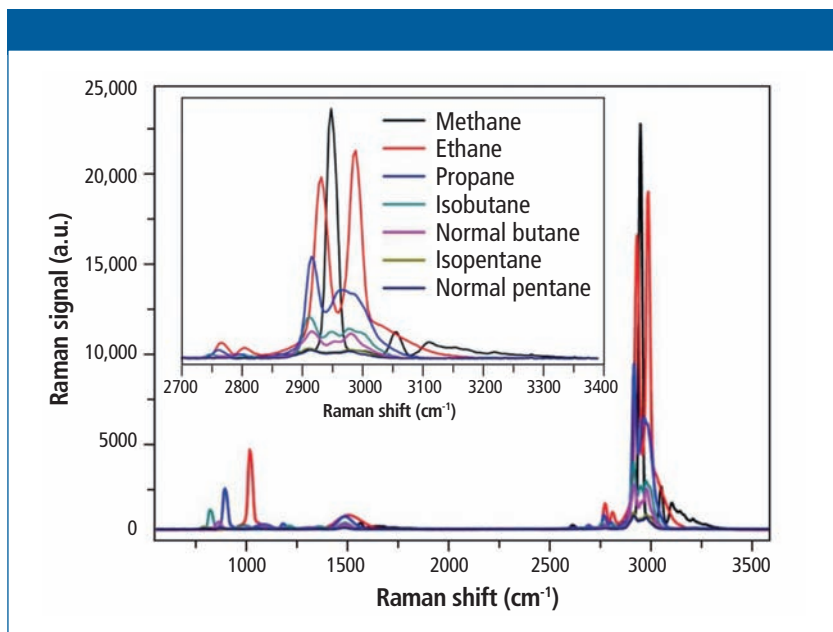


Figure 2: Raman spectra for the seven hydrocarbon gases under study, illustrating the high degree of overlap of the spectral bands key for identification and discrimination of each component. Adapted with permission from reference 5, copyright 2017 Elsevier.

phase holographic (VPH) grating in an aberration-corrected transmissive design with a thermoelectrically cooled Hamamatsu charge coupled device (CCD) detector (1024 x 64 pixels). Free-space coupling to the spectrometer's 25- μm slit was chosen to maximize use of the $f/1.3$ aperture for maximum sensitivity, thus enabling short integration times while maintaining spectral resolution of $\sim 9\text{ cm}^{-1}$.

Laser light was delivered to the gas cell via a longpass dichroic beamsplitter designed to reflect the 532-nm laser and pass the Raman scattered light while excluding Rayleigh scattering (Figure 1). A 20-mm focal length lens focused laser light into the gas cell through a sapphire window, also collimating emitted Raman scattering for transmission through the longpass

dichroic. The telescope in the laser path expanded the beam to enable a tighter focus of laser light into the gas cell. Rayleigh scattering in the signal path was further suppressed by a longpass filter, after which the Raman scattered light was focused onto the 25- μm entrance slit of the spectrometer by a 30-mm focal length achromatic lens. Throughout the measurements, the gas cell temperature and pressure were monitored, and pressure-flow was precisely controlled using regulator valves.

Using this gas analysis system, static measurements of 164 standard gas mixtures were performed, in addition to continuous measurements at two mud-logging sites. The standard gas mixtures were divided into three groups, all provided by Messer China

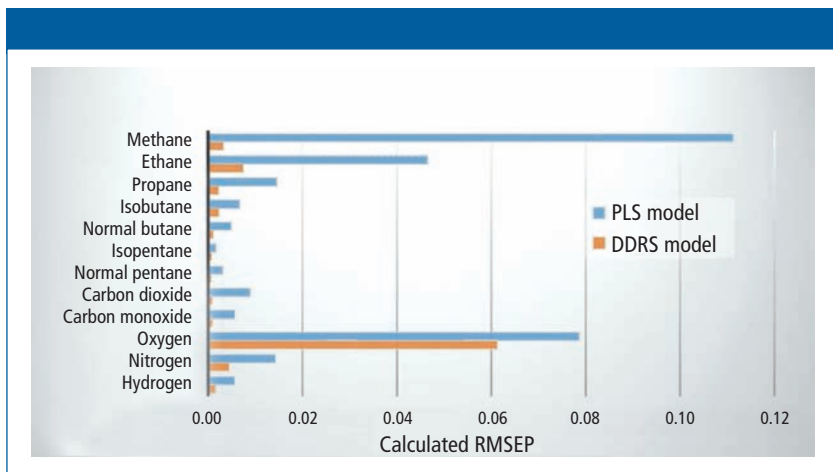


Figure 3: Comparison of root mean square error of prediction (RMSEP) values for each of the 12 component gases under study as calculated for plain PLS modeling versus DDRS modeling.

Ltd. The first group of 74 samples was composed of hydrocarbons, and included seven alkanes: methane, ethane, and propane at 0.01–20%, isobutane and normal butane at 0.01–6%, and isopentane and normal pentane at 0.01–1.6%. The second group of 52 samples was composed of nonhydrocarbons and included CO₂, CO, N₂, and H₂ in concentrations of 0.01–10.5%. In both cases, the distribution of concentrations in the samples were assigned following the principle of uniform design to simulate practical mug-logging gas samples. An additional 38 samples of O₂ gas were tested separately because of the risk of explosion. Of the total 164 sample mixtures, 19 were chosen randomly for use as an independent validation set, and the remainder were used for training the models.

Individual spectra collected for each of the seven hydrocarbon gases exhibit unique signatures (Figure 2), but because of their similar bond

structure, many of their Raman bands overlap closely. This overlap is problematic for detecting low concentrations of heavier hydrocarbons like butane and pentane, which are easily swamped by the more abundant, lighter gases. As a result, the spectra of the representative standard gas mixtures show Raman activity in similar bands, but with distinct spectral differences indicative of their differing compositions. The nonhydrocarbon gases, in contrast, were easily discriminated from one another in mixture, because of their well-separated peaks.

Results and Discussion

PLS Versus DDRS:

Analysis of Standard Mixtures

To properly assess the success of the newly developed DDRS analysis method, it was compared against plain PLS modeling for the standard gas mixtures. For each of the 12 target gases, PLS modeling was performed and evaluated. The number of PLS

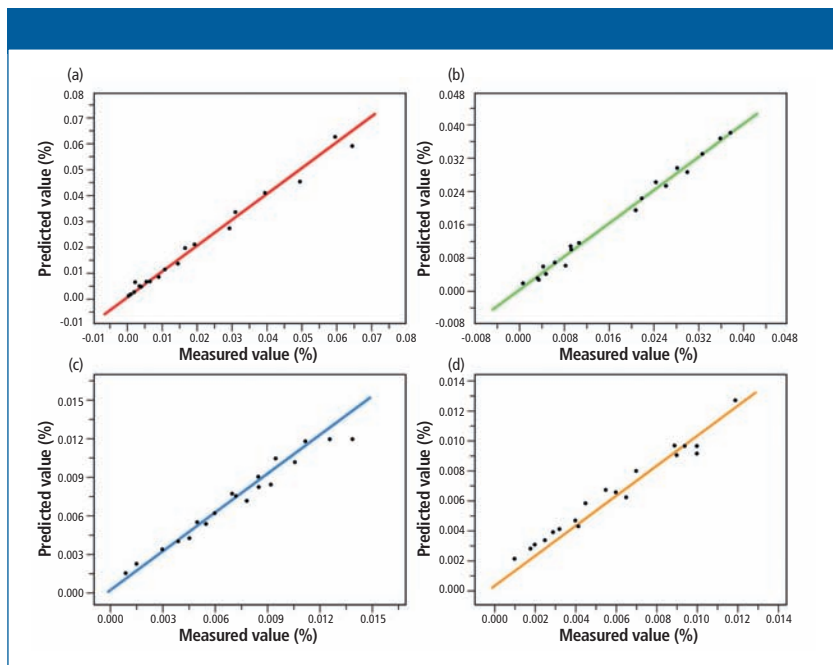


Figure 4: Measured versus predicted values for (a) isobutane, (b) normal butane, (c) isopentane, and (d) normal pentane as calculated by the DDRS model. Adapted with permission from reference 5, copyright 2017 Elsevier.

factors varied from 2 to 10, and yielded poor prediction precision in general, with root mean square error of prediction (RMSEP) values of up to 0.1113 and R values in the range 0.708–0.996 (Figure 3). Given the high number of PLS factors required and the overall poor quality of fit, PLS alone did not deliver the precision or robustness needed for accurate, reliable detection of multiple gas components in mud logging.

The same spectra were then reanalyzed using multivariate calibration models under the newly developed DDRS methodology. First, concentrations of the gases in each mixture type (hydrocarbon versus nonhydrocarbon) were assigned according to the principles of uniform design.

Then HDWT was performed on each Raman spectrum, setting the decomposition scale to 6. After the sampling probability of each HDWT coefficient for the TOFA was calculated, the parameters of the TOFA were set. After 20 iterations, the TOFA results were collected in a matrix, and the frequency of each variable was calculated. This approach allowed a series of PLS models to be constructed with an increasing number of most frequent variable, from which the PLS model with minimum RMSEP was selected as the final model.

Looking at the results of modeling each target gas component (Table I), it can be seen that DDRS delivers high prediction precision with a relatively low number of required variables

and only two PLS factors. RMSEP values are significantly lower across the board for DDRS versus plain PLS modeling (Figure 3), while R values were consistently >0.969 , indicating a much better quality of fit. Additionally, an F-test to compare the two approaches confirmed that DDRS is a significantly better calibration model for component analysis in the gas mixtures.

In terms of practical applicability, it is important that DDRS address the particular challenges of applying Raman spectroscopy to mud-logging gas analysis. Firstly, it must be able to successfully isolate a single gas target from within a highly overlapped and unpredictable matrix. This requirement is well evidenced by the results for methane, for which prediction results were improved tremendously by DDRS. Secondly, the model must be capable of quantifying low concentrations of heavier alkanes such as butane and pentane in mixtures dominated by lighter components. DDRS also performed extremely well in this respect, as can be seen by the excellent agreement between predicted and measured values for isobutane, normal butane, isopentane, and normal pentane (Figure 4).

With confidence in DDRS established, the limit of detection (LOD) for each target gas component was calculated according to the International Union of Pure and Applied Chemistry (IUPAC) (8), using pure helium in the system as a measure of the baseline noise. This approach yielded LOD values for the target gases of 0.012–0.086% (Table I), which are sufficiently sensitive to be relevant in the mud-logging industry.

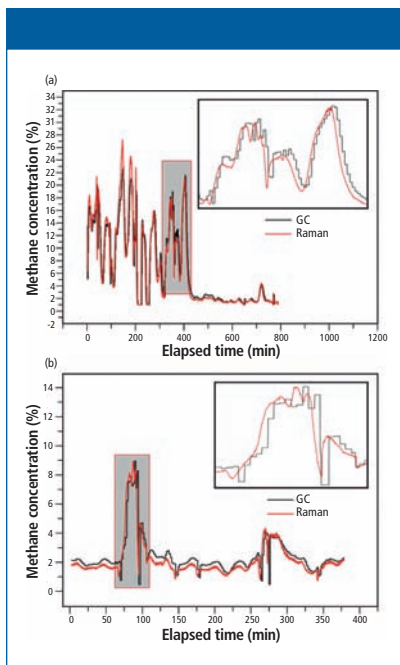


Figure 5: Comparison of GC (black curve) and Raman gas analysis system (red curve) results for methane, as measured at two mud-logging sites, (a) for 13 h, and (b) for 6 h. Adapted with permission from reference 5, copyright 2017 Elsevier.

DDRS Versus GC: A Comparison in the Field

Having established the capability of DDRS to quantify the target gas components within simulated gas mixtures, the method was benchmarked against the industry standard method of GC at two actual mud-logging sites. For this purpose, the system was connected serially between the extractor and GC system (CPS-KQ-VI, Shanghai China Petroleum Instrument Co., Ltd.) at each site, using a small Raman gas cell volume to minimize gas sample delay between the measurements. The extracted gas was measured for methane, first by the DDRS system

(every 6 s), then by the GC system (every 2 min). Measurements were taken for 13 h at the first site and for 6 h at the second (Figure 5). In both cases, DDRS measurements tracked very closely with GC results, providing much faster results and with better time resolution. This speed of analysis is particularly important for the detection of thin or hidden hydrocarbon reservoirs, and represents a significant tangible benefit for use in mud logging.

Conclusion

The use of a high-sensitivity Raman system in combination with a newly developed analysis methodology termed DDRS shows multiple benefits for multicomponent gas analysis in the mud-logging industry. DDRS makes use of higher-density wavelet transform (HDWT) together with template oriented frog algorithm (TOFA) to find an optimal combination of spectral features with minimum overlap, and then constructs high-quality calibration models for gas analysis. Its ability to isolate both hydrocarbon and nonhydrocarbon target gas components within an uncontrolled and variable matrix with high prediction accuracy makes it a promising analysis method at mud-logging sites. When tested under the rigors of two real-world mud-logging sites, DDRS compared favorably with GC. In delivering much faster, better resolved measurements, the system shows excellent potential for high-throughput analysis of multiple gas components in real time, which could be extended to online multicomponent analysis in many other gas and fuel systems.

References

- (1) D. Klaus and L. Bierenriede, *Oil-Gas Eur. Mag.* **41**, 118–126 (2015).
- (2) S.J. Maguireboyle and A.R. Barron, *Environ. Sci.-Proc. Imp.* **16**, 2237 (2014).
- (3) S.A. Barclay, R.H. Worden, J. Parnell, D.L. Hall, and S.M. Sterner, *AAPG Bull.* **84**, 489–504 (2000).
- (4) D.E. Diller and R.F. Chang, *Appl. Spectrosc.* **34**, 411–414 (1980).
- (5) X. Han, Z. Huang, X. Chen, Q. Li, K. Xu, and D. Chen, *Fuel* **207**, 146–153 (2017).
- (6) Y. Hu, T. Jiang, A. Shen, W. Li, X. Wang, and J. Hu, *Chemometr. Intell. Lab.* **85**, 94–101 (2007).
- (7) I.W. Selesnick, *IEEE T. Signal Proces.* **54**, 3039–3048 (2006).
- (8) M. Safaeian, D. Solomon, and P.E. Castle, *Spectroscopy* **18**, 112–114 (2003).

Da Chen is a professor of Biomedical Engineering at the College of Precision Instrument & Opto-Electronics Engineering at Tianjin University in China. **Cicely Rathmell** is the vice president of marketing at Wasatch Photonics in Durham, North Carolina. Direct correspondence to: marketing@wasatchphotonics.com ■

For more information on this topic,
please visit our homepage at:
www.spectroscopyonline.com

Flash Photonics Frontiers of Spectroscopy

We sell ready-made and custom Raman Systems.

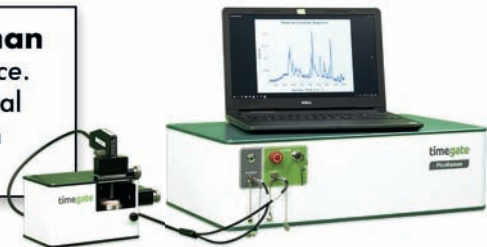


MarqMetrix® All-in-One with patented BallProbe

Highly accurate Raman measurements in less than 5 minutes out of the box.

TimeGate PicoRaman

Faster than Fluorescence.
World's first commercial time-resolved Raman spectrometer.



TSI EZRaman Handheld

High performance handheld Raman analyzer.

Wasatch Photonics

The WP $f/1.3$ optical bench design enables the world's fastest Raman spectrometers.



Unique project?

Flash Photonics designs and builds custom Raman systems with industry leading sources, components, and detectors.

Exploring the Unknown with Correlative Raman Imaging and Scanning Electron Microscopy

It's said that "seeing is believing." Unfortunately no single imaging technique can reveal every feature of a sample because each relies on a different interaction with the material being investigated. A more comprehensive understanding can be achieved by using several techniques and correlating the results. This advantage is particularly pronounced when using methods that, on the one hand, deliver images of the morphology of a sample and, on the other hand, give information suitable for determining its molecular composition. Confocal Raman imaging and scanning electron microscopy are techniques that are ideally suited to correlating structural and chemical information as shown here on a variety of samples.

Guillaume Wille, Karin Hollricher, and Ute Schmidt

As has been demonstrated in the past, correlating morphological, molecular, and chemical properties from the same region of interest (ROI) of a complex specimen yield a much better understanding than confining oneself to studying only one of these characteristics. On the micrometer or even nanometer scale, the use of two complementary microscope technologies is the method of choice for such a thorough analysis. Over the past decade, high-performance analytical techniques relevant to correlative microscopy have come to include optical microscopy, scanning elec-

tron microscopy (SEM), atomic force microscopy (AFM), tomography, energy dispersive X-ray spectroscopy (EDS), focused ion beam (FIB), and secondary ion mass spectrometry (SIMS), among others. For example, the combination of a confocal light microscopy and electron microscopy (CLEM) has been used more, especially in cell biology, to characterize not only fixed but also living cells in great detail (1).

The combination of SEM-EDS and Raman imaging is an ideal correlative technique for many applications. It includes SEM's ability to image structural surface features of a specimen

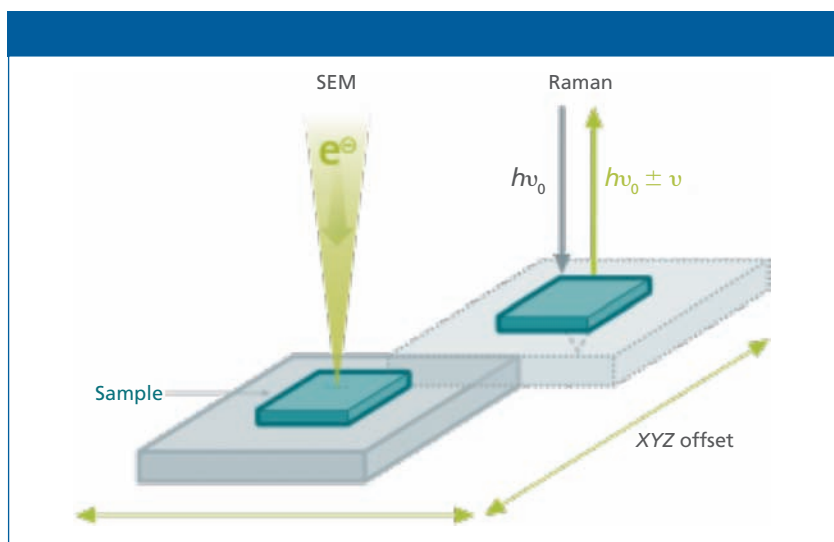


Figure 1: The principle of correlative Raman-in-SEM imaging. For easy correlation of Raman and SEM images, a setup was developed that allows Raman imaging within the vacuum chamber of a stand-alone SEM system. The samples are automatically transferred from one measuring position to the other, streamlining the workflow and drastically improving the instrument's ease of use.

at extremely high resolution, down to 1 nm, with a remarkable depth-of-field, resulting in images of great three-dimensional (3D) structural detail. EDS, often incorporated in an SEM system, can identify the chemical elements of the sample. Additionally, Raman spectroscopy can identify the sample's molecules and their characteristics. By acquiring a Raman spectrum at every pixel of the ROI, a Raman image can be generated, visualizing the local distribution of the constituent molecules, degree of crystallinity, crystal symmetry and orientation, and stress and strain states in the sample. The resolution of this technology is diffraction limited to about 150 nm. The three technologies—SEM, EDS, and Raman imaging—are well established and robust (2,3). The development of approaches

for correlative Raman imaging and SEM has been described elsewhere (4).

Materials and Methods

Since the first Raman-SEM instrument was assembled from home-built parts nearly 20 years ago, the development of Raman-SEM systems has significantly advanced to meet the requirements of scientists. Retrieving the ROI, which had long been a tedious and difficult procedure, has been made easy by locating the Raman unit within the SEM vacuum chamber and guiding it with integrated software. By automatically transferring the sample between the electron beam and the Raman microscope within the vacuum chamber, confocal Raman imaging can be performed without compromising SEM performance (5). Here, correlative Raman imaging-SEM (named RISE

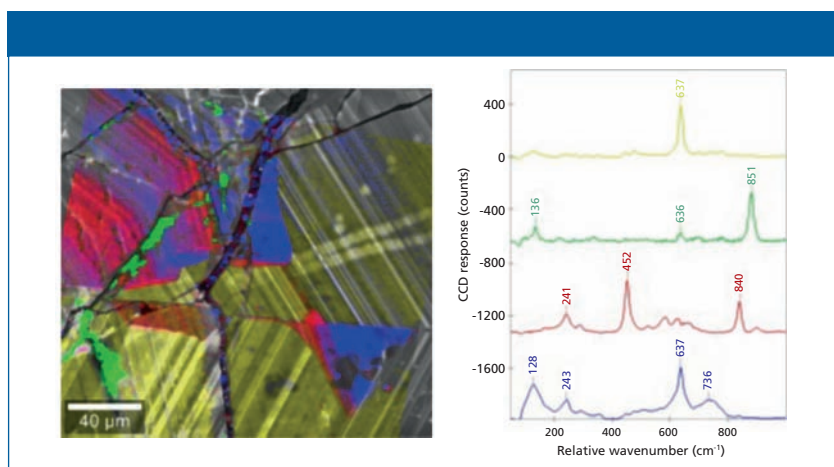


Figure 2: Raman-SEM image of cassiterite. The confocal Raman image that was generated based on the spectrum of each pixel of the ROI was superimposed onto a CL image of the same area. The Raman bands at 638 and 741 relative wavenumbers identify SnO_2 while the other spectra with additional Raman bands result from additional elements and varying lattice compositions in the crystal. Raman image parameters: $200 \times 200 \mu\text{m}^2$; 200×200 spectra, integration time of 80 ms per spectrum, 1 mW laser power.

microscopy) was performed with several systems. In all of them, the objective and the scanning stage of a confocal Raman microscope (apyron, WITec) was located inside the vacuum chamber of the SEM. The location of the objective is offset from the SEM column, thus freeing space for other detectors that require the electron beam within the small chamber. After EDS and SEM imaging, the sample is simply transferred to the Raman measuring position using the SEM stage (Figure 1). Samples are automatically transferred from one measuring position to the other and stay within the vacuum chamber of the SEM system for the entirety of the procedure, thus streamlining the workflow and drastically improving the instrument's ease of use.

Two different SEM systems (Mira, Tescan, and Sigma 300, ZEISS) were

used for the analysis of cassiterite and pearl, and hematite, respectively.

The Raman systems were equipped with a spectrometer (UHTS 300, WITec), a 100x vacuum objective (N.A. 0.75) and a 532-nm excitation laser. Raman spectra were analyzed with multivariate spectral analysis methods (6).

Inspection of Cassiterite

Cassiterite (SnO_2) is the main source of tin (Sn) and has been extensively studied. In this ore, Sn is often associated with other metals such as titanium (Ti), niobium (Nb), tantalum (Ta), indium (In), and tungsten (W). These elements can be identified and distinguished from SnO_2 by Raman imaging. SnO_2 has characteristic Raman bands at 638 and 741 relative wavenumbers (Figure 2). The inclusion of other elements as well as vari-

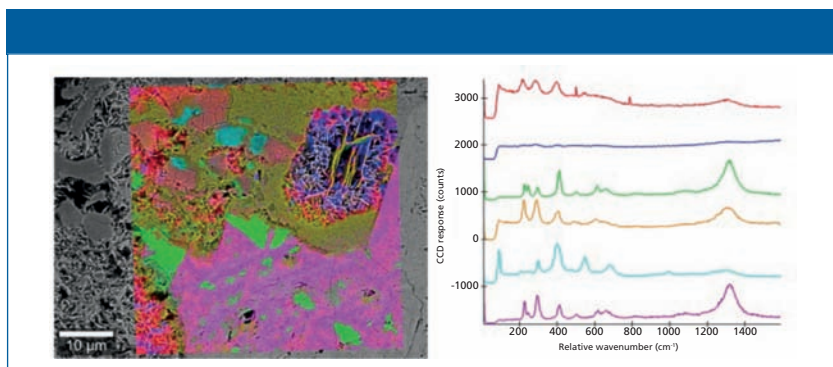


Figure 3: Raman-SEM image of hematite. The analyzed sample consists of several crystal forms of hematite (red, blue, green, orange, pink) and of goethite (light blue, cyan). The Raman image was derived from the Raman spectra acquired with the Raman microscope of the combined Raman-SEM system and overlaid onto the SEM image. Raman image parameters: 50 x 50 µm²; 150 x 150 spectra, integration time of 150 ms per spectrum, 10 mW laser power.

ations in the crystal lattice structure influences this typical spectrum. For example, the Raman band at 840 relative wavenumbers (red spectrum in Figure 2) is produced by a vibrational mode of Nb. SEM and cathodoluminescence (CL) imaging were used to determine the precise ROI, EDS identified trace elements, and the following Raman analysis showed the distribution and crystal orientations of the molecules in the SnO₂ crystal (7). This example also convincingly illustrates that confocal Raman imaging can be a quick procedure: The confocal Raman image comprising 40,000 pixels was acquired in less than 1 h and displays both very high spectral sensitivity and local resolution simultaneously.

Iron Ore Analysis

Iron ore contains many minerals, including variations of iron oxide. Thus, before processing iron ore, an extensive mineralogical characterization is required. Today, this characterization is done by optical

microscopy and SEM (8). Differentiation of iron ore minerals that have similar oxygen contents with SEM is difficult. However, Raman spectroscopy can easily distinguish iron oxides from one another. Here, a piece of hematite (Fe₂O₃) was analyzed first with SEM, then with the integrated confocal Raman microscope as shown in Figure 3. SEM admittedly depicts some structural characteristics, but cannot differentiate between the oxides. However, the Raman spectra indicate the occurrence of several crystal forms of hematite and goethite (FeO(OH)). The distribution of these minerals is shown in the Raman image that has been overlaid onto the SEM image.

A Pearl's Shell

The shiny opalescence of pearls results from the mineral aragonite, an orthorhombic polymorph of calcium carbonate that is produced by a biomineralization process. This structure can be visualized with SEM. Some

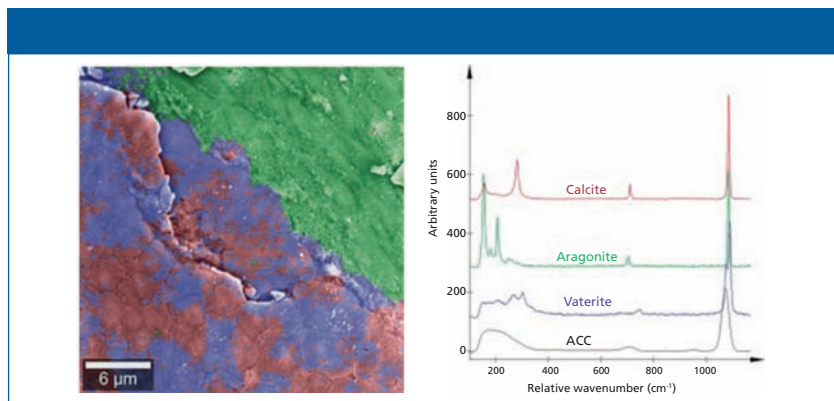


Figure 4: Raman-SEM imaging of a pearl's surface. Raman spectroscopy can differentiate not only aragonite (blue, red) and vaterite (green), two polymorphs of calcium carbonate, but also different phases of aragonite in the pearl. The image is an overlay of the SEM image of the pearl's surface with the confocal Raman image that was created from the Raman spectra at each pixel of the ROI. Raman image parameters: 40 x 40 μm^2 ; 150 x 150 spectra, integration time of 100 ms per spectrum, 5 mW laser power.

pearls show biomineralization defects characterized by reduced iridescence (also called “milky pearl”) (9). These defects are related to the change in the mineralization form of calcium carbonate, from orthorhombic aragonite to hexagonal vaterite. Such a defect was studied with correlative Raman imaging and SEM. The crystallographic structures of the two polymorphs are indicated in the SEM image (Figure 4). The polymorphs have different Raman spectra, so they can be easily identified, imaged, and correlated with the morphology determined from the SEM data. Furthermore, small changes in relative Raman peak intensities highlight anisotropies in the aragonite phase.

Conclusion

Here, the feasibility and usefulness of correlative Raman imaging and scanning electron microscopy was explored on several samples, namely cassiterite, hematite, and CaCO_3 poly-

morphic components of a pearl. All three example measurements reveal the power of Raman imaging as a complementary method to EDS in the determination of the molecular composition of minerals. The locating of trace elements in the cassiterite sample by combining confocal Raman imaging with SEM and EDS imaging is demonstrated. The sensitivity of Raman imaging to polymorphism and small changes to crystal lattice vibrations is highlighted in the measurements on iron ore and pearl. Because Raman imaging reveals the kind of molecules in a sample and their locations in detail, these chemical data can be precisely correlated with the morphological features revealed by high-resolution electron microscopy and the elemental distribution obtained by EDS.

References

- (1) A.B. Mironov, *J. Microsc.* **235**, 308–321 (2009).

- (2) D. Goldstein et al., *Scanning Electron Microscopy and X-Ray Microanalysis*, 3rd Ed. (Springer, Heidelberg, Dordrecht, London, and New York, 2003).
- (3) O. Hollricher, *Confocal Raman Imaging*, J. Toporski, T. Dieing, and O. Hollricher, Eds. (Springer Int. Publishing, Cham [CH], 2018).
- (4) C. Cardell and I. Guerra, *TRAC, Trends Anal. Chem.* **77**, 156–166 (2016).
- (5) J. Jiruse, M. Hanicinec, M. Havelka, O. Hollricher, W. Ibach, and P. Spizig, *Microsc. Microanal.* **20**, 990–991 (2014)..
- (6) T. Dieing and W. Ibach, *Software Requirements and Data Analysis in Confocal Raman Microscopy*, 2nd Edition, J. Toporski, J. Dieing, and O. Hollricher, Eds., (Springer Int. Publishing, Cham [CH], 2018).
- (7) G. Wille, C. Lerouge, and U. Schmidt, *J. Microscopy Vol.* **270**, 309–317 (2018).
- (8) E. Donskoi, J. Manuel, P. Austin, A. Poliakov, M. Peterson, and S. Hapugoda, *Appl. Earth Sci.* **122**, 217–229 (2013).
- (9) X.E. Bourrat, *Mater. Charact.* **72**, 94–103 (2012).

Karin Hollricher and **Ute Schmidt** are with WITec GmbH in Ulm, Germany. **Guillaume Wille** is with BRGM in Orleans, France. Direct correspondence to: Ute.Schmidt@WITec.de ■

For more information on this topic, please visit our homepage at: www.spectroscopyonline.com

Continued from page 33

References

- (1) K. Sato, *Crystallization of Lipids: Fundamentals and Applications in Food, Cosmetics, and Pharmaceuticals* (John Wiley & Sons, Hoboken, New Jersey, 2018).
- (2) S. Bresson, D. Rousseau, S. Ghosh, M. El Marssi, and V. Faivre, *Eur. J. Lipid Sci. Technol.* **113**, 992–1004 (2011).
- (3) R. Wille and E. Lutton, *J. Am. Oil Chem. Soc.* **43**, 491–496 (1966).
- (4) K. Dewettinck, I. Foubert, M. Basiura, and B. Goderis, *Cryst. Growth Des.* **4**, 1295–1302 (2004).
- (5) C. Loisel, G. Keller, G. Lecq, C. Bourgaux, and M. Ollivon, *J. Amer. Oil Chem. Soc.* **75**, 425–439 (1998).
- (6) A.G. Marangoni and S.E. McGauley, *Cryst. Growth Des.* **3**, 95–108 (2002).
- (7) K. van Malssen, A. Langevelde, R. Peschar, and H. Schenk, *J. Amer. Oil Chem. Soc.* **76**, 669–676 (1999).
- (8) R.G. Snyder, H.L. Strauss, and C.A. Elliger, *J. Phys. Chem.* **86**, 5145–5150 (1982).
- (9) R.J. Meier, *Polymer* **43**, 517–522 (2002).
- (10) M. Zheng and M. Du, *Vib. Spectrosc.* **40**, 219–224 (2006).

Nathan C. Crawford and **Rui Chen** are with Thermo Fisher Scientific in Madison, Wisconsin. **Mohammed Ibrahim** is with Thermo Fisher Scientific in San Jose, California. Direct correspondence to: nathan.crawford@thermofisher.com ■

For more information on this topic, please visit our homepage at: www.spectroscopyonline.com



Slide Sample Holder for Raman and SERS

Anne-Marie Dowgiallo, PhD, Ocean Optics

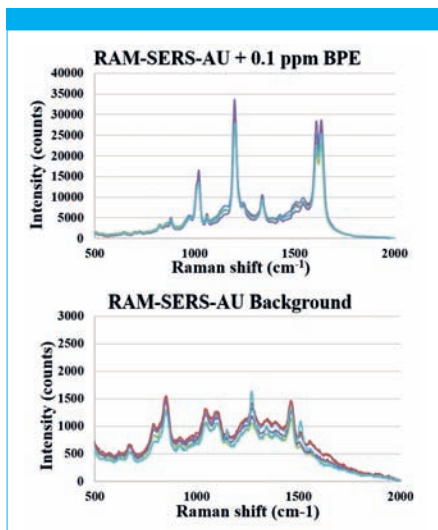
The newest Raman sample holder from Ocean Optics, the RM-SERS-SHS, accommodates surface enhanced Raman spectroscopy (SERS) substrates. RM-SERS-SHS measures Raman spectra of samples deposited on SERS substrates by connecting a probe to the holder.

The RM-SERS-SHS is made of aluminum and stainless steel, and is used with 12.7 mm Raman probes. A set screw connects the probe to the holder and holds it in place for highly reproducible positioning. The base can be fixed on an optical table, or disassembled, which reduces the footprint. The clamped SERS substrate is convenient for handheld measurements.

Experimental Conditions

A modular Raman system was used, consisting of 785 nm laser excitation, Raman probe, and thermoelectrically cooled CCD detector. An integration time of 3 s and laser power of 15 mW were used. Measurements were performed by inserting a SERS substrate (RAM-SERS-AU) with and without analyte (0.1 ppm BPE) into the holder and collecting the Raman spectrum. This was repeated to show the reproducibility of the measurement.

Results



Conclusions

The new substrate holder provides accurate positioning for the Raman measurement, avoids the influence of ambient light, and improves the accuracy of the Raman measurement.

Ocean Optics

8060 Bryan Dairy Rd., Largo, FL 33777

tel. (727) 733-2447

Website: www.oceanoptics.com

Extending Raman's reach

Today's Raman spectroscopy demands higher signal, less noise, & faster measurements than ever before. We deliver.

- ▶ Spectrometers & systems, 405 – 1064 nm
- ▶ Configurable, from coupling to cooling
- ▶ Seeing is believing – try a demo!



Wasatch) Photonics

UV-VIS | RAMAN | FLUORESCENCE | NIR

+1 919-544-7785 • info@wasatchphotonics.com

wasatchphotonics.com

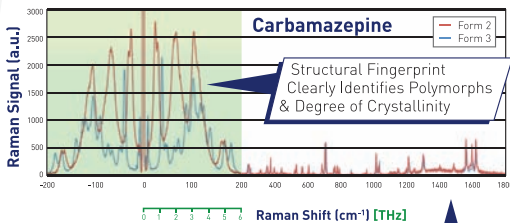
SEE WHAT YOU'VE BEEN MISSING WITH THz-RAMAN[®]

RAMAN SPECTROSCOPY PRODUCTS

Structural Fingerprint

Chemical Fingerprint

Ultra-low Frequency THz-Raman[®] Systems & Accessories



Both Stokes and anti-Stokes signals down to 5cm⁻¹

Complete chemical fingerprint



High Throughput Screening



In-situ Process Probes



Transmission Mode for Bulk Testing



Microscope/Benchtop



SureLock[™]

Wavelength Stabilized Lasers 405nm to 1064nm

MINI-BENCHTOP



TURNKEY MODULES



OEM SOLUTIONS



COMPONENTS



Ondax patented THz-Raman[®] Spectroscopy Systems extend the reach of your Raman system down into the low frequency/THz regime, unveiling a secondary "structural fingerprint" that can be used to clearly differentiate polymorphs, monitor and quantify crystallinity, or enhance forensic analysis of materials – all while maintaining the complete chemical fingerprint. See what you've been missing with THz-Raman[®]!